

Developement of a Detector for Bound Quantum States of Neutrons in the Earths Gravitational Field

**This diploma thesis has been carried out by
SOPHIE LOUISE NAHRWOLD
at the Physics Institute of the University of Heidelberg
under the supervision of
PRIV.-DOZ. DR. HARTMUT ABELE.**

Abstract

It was a great challenge to produce a position sensitive neutron detector with a spatial resolution below $3\mu m$, since ordinary position sensitive neutron detectors have resolutions of $100\mu m$, at best. The goal was met and the new detector was put to test this summer during an experiment investigating the behaviour of ultra-cold neutrons in the earths gravitational field. The detector was used to measure the density distribution of these neutrons above a horizontal mirror. The resolution of the detector was determined from a quantum mechanical fit of the data and has turned out to be $1.4\mu m$!

Additionally, a number of systematical checks were performed on data obtained from the gravitational levels experiment of 2002. The relative accuracy of the determination of the earths gravitational acceleration was determined to be 2% and the effect of additional, gravity-like forces was investigated.

Zusammenfassung

Es war eine große Herausforderung einen ortsauflösenden Neutronen Detektor mit einer Auflösung unter $3\mu m$ zu entwickeln, da solche Detektoren normalerweise nur eine Auflösung von maximal $100\mu m$ erreichen. Dieses Ziel wurde erreicht und der Detektor wurde in diesem Sommer bei einem Experiment zur Untersuchung gebundener Quantenzustände von Neutronen im Gravitationsfeld der Erde getestet. Mit dem Detektor wurde die Dichteverteilung der Neutronen über einem horizontalen Spiegel gemessen und seine Auflösung dann mit Hilfe eines quantenmechanischen fits an die Daten zu $1.4\mu m$ bestimmt!

Desweiteren wurden im Rahmen dieser Arbeit einige systematische Untersuchungen zu Daten des Gravitationsexperiments von 2002 durchgeführt. Die relative Genauigkeit bei der Bestimmung der Erdbeschleunigung wurde untersucht und beträgt 2%. Einige Tests zu den Auswirkungen zusätzlicher, gravitationsähnlicher Kräfte wurden unternommen.

Contents

1	Introduction	1
1.1	Early observation of gravitational quantum effects	2
1.2	Free fall in quantum mechanics	3
1.3	Our experiment	5
1.3.1	Two approaches to the bound states measurement . .	9
2	Measurement of the density distribution of the neutrons	13
2.1	The setup and the derivation of the fitting function	13
2.2	Treatment of the data from the position sensitive detector . .	17
2.2.1	Correction of the data using the "edge"	18
2.2.2	Correction of the data by minimizing the width of the distribution	21
2.3	Comparison of the Uranium and Boron coated detector . . .	25
2.4	Classical versus quantum mechanical interpretation of the measurement	28
3	The Boron coated, position sensitive detector	33
3.1	The uncoated CR39 trace detectors	33
3.2	Identification of the traces in the CR39 detector	35
3.3	The application of the ^{10}B coating	38
3.4	The treatment of the irradiated detectors	40
3.5	The resolution of the detector	41
3.6	Detection principle and efficiency	43
3.7	Background	47
3.8	Reading out the detectors	47
4	A quantum mechanical determination of the earths gravitational acceleration	49
4.1	Fitting g	49

5	Testing for deviations from Newtonian gravity	55
5.1	Introduction	55
5.2	The Yukawa potential for our setup	57
5.3	An Estimation of possible limits for the parameters of the Yukawa potential	60
5.4	An investigation of systematic effects on our limits for α and λ	61
5.4.1	Observation of different effects for attractive and repulsive Yukawa potentials	62
5.4.2	Effects of a systematic error of the data	63
6	Summary	67
A	A recipe for handling the detectors	69
A.1	Cleaning	69
A.2	Coating	69
A.3	Storage	70
A.4	Removing the coating	70
A.5	Etching	70
A.6	Readout	70
B	Ultra-Cold Neutrons	71
	Bibliography	75

Chapter 1

Introduction

Gravity is one of the four fundamental forces that govern the structure of the universe as we know it and, by now, it is probably the most exotic one. While the other three interactions can be described by a single quantum theory gravity has stubbornly resisted unification attempts for decades. Its formulation by the theory of general relativity is, albeit a gauge theory, distinctly different from the description of all other interactions and here we can see gravity as a property of space and time themselves and not as something that simply exists in there. Yet, gravity is also, together with electromagnetism, a phenomenon that is accessible to the direct investigation by human beings. Every child will at one point in his or her life start to let things drop intentionally, presumably to find out whether or not really everything will end up on the floor.

At very large scales gravity has been investigated very thoroughly by many specialists. General relativity is now part of our everyday lives in the form of GPS systems, its predictions have been tested by the investigation of pulsars and neutron stars and, recently, astronomers have found strong indications that there is indeed a black hole at the center of our galaxy. Newtonian gravity is, of course, also well tested. The strength of the gravitational force, the equivalence of heavy and inert mass and the inverse square law of the gravitational force have been probed over and over again with ever greater accuracy.

The one aspect of gravity that is comparatively unexplored is its behaviour over very short distances and the interaction of very small masses, i.e. the quantum mechanical regime. Conducting experiments in this area is quite challenging because gravity is so weak compared to the other interactions which have to be shielded off very effectively. This can be a difficult task to achieve in practice. The general interest in this field of experimentation, however, is great because modern, string-inspired theo-

ries aiming to achieve a unified description of all fundamental interactions predict deviations from the Newtonian inverse square force law for distances below 1mm, see for example [Ark98], [Ant98], [Ark99] or [Flor99]. These phenomena are generally summed up under the term "fifth force" and some of the corresponding theories predict effects that could be falsified by this experiment which is designed to measure the shape of bound state wave functions of neutrons in the earth's gravitational field.

Neutrons are ideally suited to investigate gravity on a micrometer scale because over this range they only interact with their environment through their magnetic moment and their mass. If the experimental installation is shielded from magnetic fields it is then possible to investigate the gravitational interaction isolated from all others. This is a unique possibility since atoms and rigid bodies would also be affected by Casimir and van-der-Waals forces which are many times stronger than gravity. Deviations from these Casimir and van-der-Waals forces due to newly predicted effects can also be measured and experiments doing this have already excluded a great range of models for possible new interactions. These experiments are discussed in [Fis01] and [Fis03], for example. In theory, a measurement of the gravitational interaction of neutrons could also be very effective, again due to the weakness of the gravitational force which would make it possible to detect even small deviations. This will be discussed in detail in chapter 5.

1.1 Early observation of gravitational quantum effects

The very first experiment to measure gravitationally induced quantum effects was conducted in 1975 by Colella, Overhauser and Werner, [COW75]. In this remarkable experiment the phase shift of thermal neutrons due to their interaction with the gravitational field was measured with a neutron interferometer. A schematic drawing of the setup taken from the original publication can be seen in figure 1.1. A nearly monoenergetic beam of neutrons was split in two by an interferometer at point A and rejoined at point D where the two beams would interfere. The phase difference between the two beams could be changed by turning the interferometer around the AB axis by angle δ , thereby altering the potential along CD by a constant factor $m_n g l_1 \sin \delta$, where m_n is the neutron mass, g the gravitational acceleration and l_1 the distance between points C and D. The phase difference between the neutrons travelling along the two different paths is

$$\Phi_{ACD} - \Phi_{ABD} = -\frac{-im_n^2 g l_1 l_2 \lambda \sin \delta}{2\pi \hbar^2}, \quad (1.1)$$

where l_2 is the distance between A and C and λ the de Broglie wavelength of the neutrons. This phase shift had been verified even then well within 1%! Nowadays atom and neutron interferometry are used in high-precision gravimetric experiments and have achieved relative accuracies of less than 10^{-9} g. With our experiment we have gone one step further, still, and we have directly observed gravitationally bound quantum states of ultra cold neutrons (UCN). This was the first time that the shape of these wavefunctions had been measured.

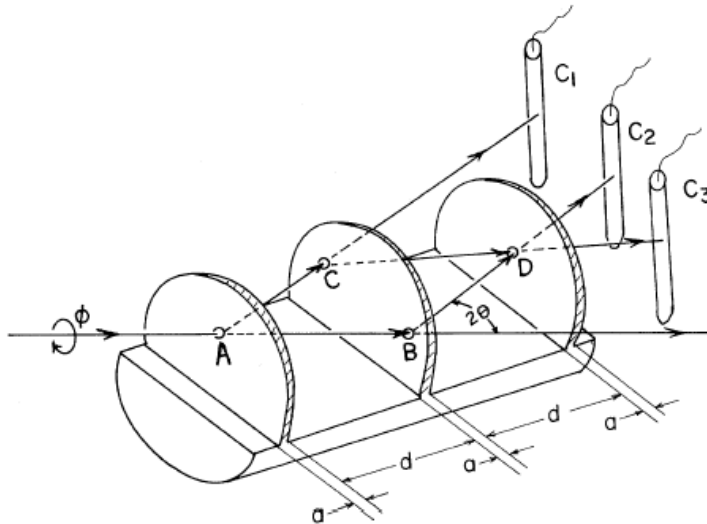


Figure 1.1: Schematic drawing of the COW experiment to detect gravitationally induced quantum interference taken from [COW75]

1.2 Free fall in quantum mechanics

To discuss our experiment in detail it is necessary to briefly review the theory of the quantum mechanical free fall, which is discussed, for example, in [Flü99]. The floor, in this problem, is a high potential barrier for $z \leq 0$ and there is a linear potential mgz for $z \geq 0$. The potential is shown in figure 1.2. The Schroedinger equation then looks like

$$\left[-\frac{\hbar^2}{2m} \frac{\partial^2}{\partial z^2} + mgz \right] \phi_n(z) = E_n \phi_n(z), \quad (1.2)$$

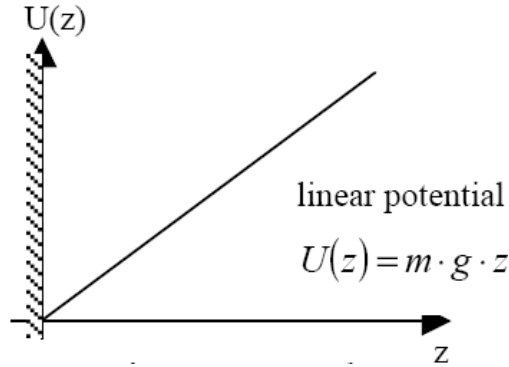


Figure 1.2: Potential of the free fall problem

with the boundary conditions

$$\phi_n(0) = 0$$

$$\phi_n(z) = 0, z \rightarrow \infty$$

for all states n . It is convenient to rescale the equation with a scaling factor R defined as

$$R = \left(\frac{\hbar^2}{2m^2g} \right)^{\frac{1}{3}} \quad (1.3)$$

so that $z \rightarrow \zeta = \frac{z}{R}$. R is the characteristic length of the system and for neutrons $R \approx 6\mu m$. Inserting this into 1.2 one obtains

$$-\frac{\partial^2}{\partial \zeta^2} \phi_n(\zeta) + \zeta \phi_n(\zeta) = \epsilon_n \phi_n(\zeta), \quad (1.4)$$

where $\epsilon_n = \frac{E_n}{mgR}$. The solutions to these equation are the Airy functions:

$$\phi_n(\zeta) = Ai(\zeta - \epsilon_n), \quad (1.5)$$

which are shown in figure 1.3. They have to fulfill the boundary conditions $Ai(-\epsilon_n) = 0$ and $Ai(\zeta - \epsilon_n) = 0, \zeta \rightarrow \infty$. A very good approximation for the ϵ_n can be obtained from the asymptotic behaviour of the Airy functions and yields

$$\epsilon_n = \left(\frac{3\pi}{2} \left(n - \frac{1}{4} \right) \right)^{\frac{2}{3}}. \quad (1.6)$$

Now the energy eigenvalues of the system are also determined:

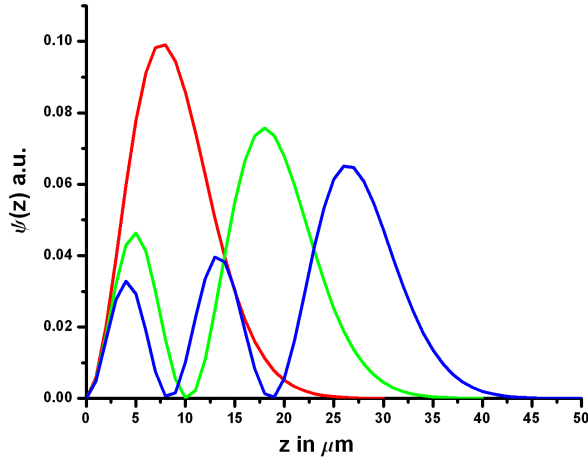


Figure 1.3: The first three bound states of the linear potential

$$E_n = mgR\epsilon_n = mgz_n, \quad (1.7)$$

where the $z_n = R\epsilon_n$ are the classical turning points of the particles trajectories. For the first few states the energy eigenvalues, the expectation values of z and the turning points of the corresponding classical trajectories are collected in table 1.1.

state number	E_n in peV	$\langle z \rangle$ in μm	classical turning point in μm
1	1.407	9.2	13.7
2	2.460	16.0	24.0
3	3.322	21.6	32.4
4	4.1	39.8	26.6

Table 1.1: Energies, expectation value of z and classical turning points of neutrons in gravitationally bound states

1.3 Our experiment

In our experiment, performed for the first time in 1999 at the Institute Laue Langevin (ILL) in Grenoble, we have observed gravitationally bound quantum states with ultra cold neutrons, see [Ne02] and [Ne03]. This is not trivial since, normally, even the energies of UCNs of about 100neV

are much higher than the eigenenergies of the gravitational bound states which are of the order of peV. It is therefore necessary to select neutrons with small vertical energy components using a collimator. This device ensures that, classically speaking, the neutrons can only travel on parabolic trajectories of a certain curvature and that their direct view of the detector at the end of the installation is blocked. A sketch of our experimental setup is shown in figure 1.4 whereas a detailed drawing can be seen in figure 1.5.

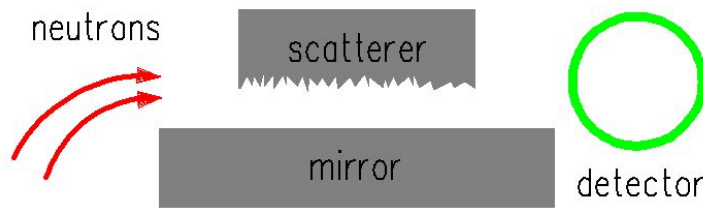


Figure 1.4: Schematic drawing of the experimental setup

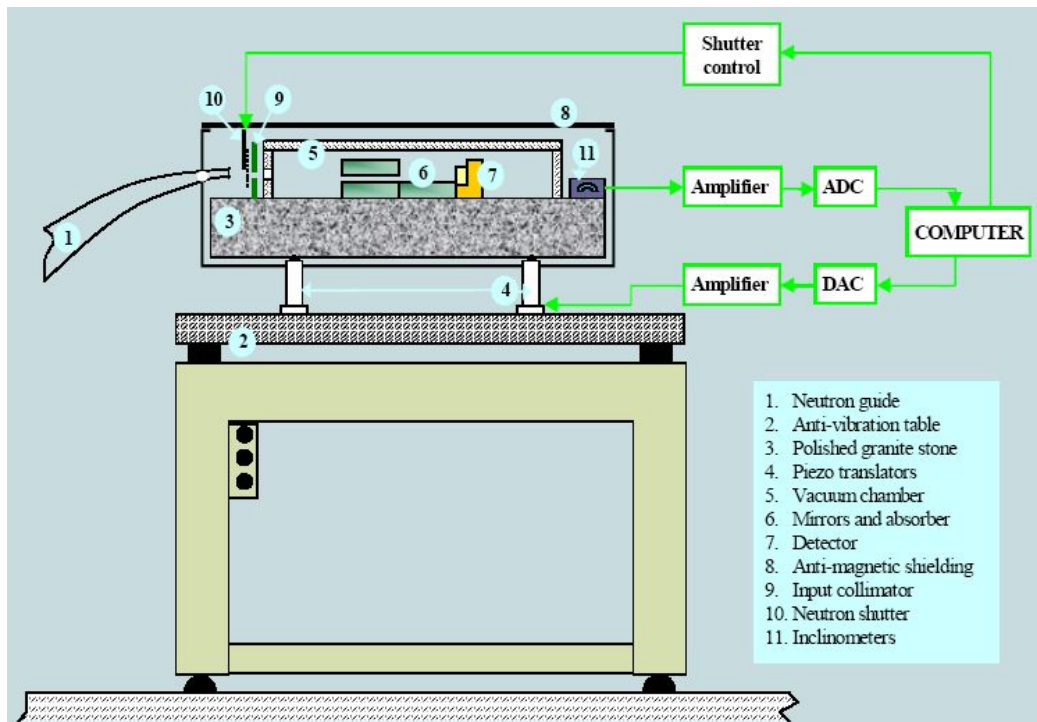


Figure 1.5: Overview of the experimental installation taken from [We01]. The "absorber" will be called scatterer for the greater part of this thesis.

The main components of the installation are one or two very flat glass mirrors topped by a scatterer and a neutron detector at the end of the mir-

rors. The neutrons interact with the mirror(s) and the scatterer via the so called Fermi potential. This is an effective potential approximated from the interaction of the neutrons with the nuclei of the surface material. Although the actual interaction of the hadrons is attractive the Fermi potential is repulsive for most materials with a magnitude of around 100neV, see appendix B for a short review of the derivation of the Fermi potential. Neutrons with energies in the same range will be reflected from these surfaces at all angles of incidence.

The mirrors we use have a roughness in the order of 0.1nm and are quite plane so that we expect neutrons to be only specularly reflected from them.

The scatterer has a roughness of several μm and is used to remove neutrons with high vertical energy components from the system. Those neutrons will occupy the higher bound states and have a greater probability to be found at higher positions, see figure 1.3. If their wave functions significantly overlap with the roughness of the scatterer they will be removed from the system. How this process works is not entirely clear. At first it was assumed that the scatterer would have to be coated with an absorbing material with low Fermi potential. Therefore the scatterer used in the first experimental run of 1999 was coated with a layer consisting mainly of Gadolinium and Titanium with a Fermi potential matched to zero, at least two orders of magnitudes below that of ordinary matter. At this point the efficiency of the scatterer was calculated using the WKB approximation for the Schroedinger equation with the Fermi potential of the absorbing layer ([We01]). The transmission through the slit between mirror and scatterer could be described by this model with only one free parameter for the overall amplitude. It was then discovered that not the material but the surface roughness was the decisive factor for the efficiency of the absorber/scatterer, which takes away the physical basis for the WKB approximation. It might also be the case that a thin layer of water molecules or some pollution of a different kind will act as an absorbing or scattering layer, making an artificial coating of the scatterer obsolete.

Our model for the interaction of UCNs with a rough surface coated with an absorbing layer is the following, [We01]: Because of their large wavelengths the neutrons passing through our installation can not resolve the microscopic roughness of the scatterer and will only see the average over the scatterers surface. The rough surface can then be described by a Gaussian error function with a width equal to the roughness of the scatterer. For a scatterer coated with an absorbing material the Fermi potential of the absorbing layer will be smeared by two such error functions, one

for the outer surface of the layer and one for the inner surface, directed towards the glass. The potential will then be proportional to a form factor

$$\partial F(z) \propto \text{Erf}\left(\frac{z-h}{\sigma\sqrt{2}}\right) - \text{Erf}\left(\frac{z-(h-d)}{\sigma\sqrt{2}}\right), \quad (1.8)$$

where h is the height of the scatterer above the mirror, σ its roughness and d is the thickness of the absorbing layer. The neutrons would see a potential of the form shown in figure 1.6 that they could penetrate leading to their absorption.

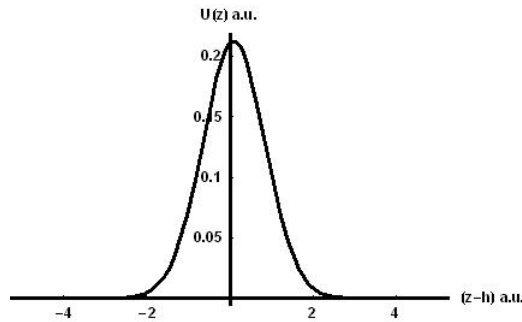


Figure 1.6: Shape of the Fermi potential of an absorbing layer applied to a rough surface

A full theoretical description of the scatterer is not yet available. It is difficult to obtain due to incoherent scattering induced by the large surface roughness. In the model used for calculations in this thesis the overlap of the wave functions with the scatterer is calculated and the efficiency of the scatterer is a free parameter. This is slightly disconcerting since this parameter basically defines the shape of the function for the neutron transmission through the installation and this has greatly limited our possibility to exclude different parameters of the fifth force, see chapter 5. Some progress has been made, however, in finding an analytical expression for the scattering parameter using scattering at hard spheres as an approximation of the true process, [We04]. The resulting parameter could not be used in our calculations, yet, because it deviated from the fitted value by 60% and could not describe the data.

1.3.1 Two approaches to the bound states measurement

The transmission measurement

There are two methods of measuring the shape of the bound state wave functions. One is to move the scatterer upwards in small steps and measure the transmission through the scatterer-mirror-system for every step. For low scatterer heights there should be no transmission through the waveguide since all bound state wave functions have a large overlap with the scatterer and the neutrons will be absorbed or scattered out of the system. Once the scatterer has reached a height of roughly $13\mu m$ where the ground state wave function has no significant overlap with the scatterer anymore, there is a sudden increase in the transmission. The transmission will then remain constant until the first excited state is clear of the scatterer and so forth. The classical expectation for this type of system would be a steady increase in transmission for all scatterer heights until the scatterer is so far out of reach that no more neutrons would be absorbed and the transmission would remain constant. The result of this measurement performed in 2002 is shown in figure 1.7 together with the quantum mechanical and classical expectations. This measurement can be considered as the first direct proof of the existence of bound quantum states in a gravitational field, see [Ne02].

The resolution here is limited by the quality of the calibration of the height h of the scatterer above the mirror which was as good as $1\mu m$ in 2002 and has been further improved for the experimental run of 2004 so that we now know h with an accuracy of about $0.1\mu m$, [Schrau04]!

The method is an integral one which means that we are measuring the integral over the distribution of the neutrons from the mirror up to the scatterer. To draw conclusions as to the shape and population of the individual states we have to differentiate. That means that we have to subtract data points from one another and that again will increase the error of the final result.

The measurement of the density distribution

The second way measure the shape of the bound state wavefunctions is a direct measurement of the neutron distribution above the mirror with a position sensitive detector. We developed a new position sensitive detector for this measurement within the framework of this thesis (see chapter 3) and conducted the measurement during the last experimental cycle, summer 2004. The results of the measurement are discussed in detail in

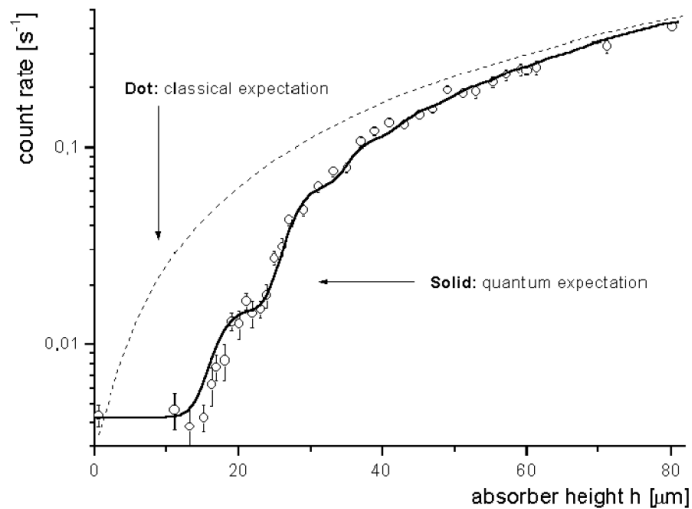


Figure 1.7: Result of the 2002 transmission measurement taken from [Abe03]. The data points give values for the neutron transmission for a certain height of the scatterer above the mirror. The solid line represents the quantum mechanical prediction for this type of measurement, the dotted line the classical prediction.

chapter 2.

The direct method is, in principle, preferable since the density matrix of the system is directly measured and all information on the shape of the bound states can be directly extracted from the data. Another advantage is that the scatterer does not play a crucial part with this method. It is used to filter out neutrons from the higher states but there is no need for the scatterer to cover all of the mirror. After the unwanted neutrons have been removed the probability distribution can be measured without the scatterer even being present. This is very fortunate since a theoretical model of the scatterer does not have a great impact on the interpretation of the data and a theoretical model of the scatterer is difficult to obtain. One problem with the interpretation of the data is that classical Monte-Carlo simulations and the quantum mechanical prediction for this measurement can be quite similar so that we could, so far, not exclude the case that we are dealing with a classical phenomenon. However, the results obtained from this measurement during the experimental run 2004 at the ILL, Grenoble are already indicative of the quantum mechanical behaviour of the neutrons.

An inconvenience concerning the direct method is that we do not have

an "online" position sensitive detector with sufficient accuracy, yet. Instead we are using nuclear trace detectors with reactive coatings that will undergo a nuclear reaction together with an incoming neutron. These detectors have to be irradiated for a certain amount of time, depending on their efficiency. Afterwards they have to be treated with some chemicals to be read out under a microscope. For a detailed description and analysis of the detectors we used see chapter 3.

Chapter 2

Measurement of the density distribution of the neutrons

In this chapter the measurement of the density distribution of the neutrons above a horizontal mirror is discussed. For this task it is essential to have a position sensitive neutron detector with a resolution below $3\mu\text{m}$. A new kind of such a detector was prepared and tested during the last year which will be discussed in chapter 3. The measurements of the density distribution were performed in summer 2004 and can be considered a significant step towards the direct observation of the quantum mechanical density distribution of neutrons above a mirror.

2.1 The setup and the derivation of the fitting function

For our measurement of the neutron distribution above the mirror the experimental configuration can be seen in figure 2.1. The gap between the scatterer and the first of the two mirrors was $30\mu\text{m}$. The step between the two mirrors was $21\mu\text{m}$. A position sensitive detector was installed directly at the edge of the second mirror. The step between the two mirrors was introduced to suppress the relative population of the ground state of the system. The reason for this is that it enhances "waviness" of the density distribution which makes it easier to distinguish between the quantum mechanical and classical predictions.

From the knowledge of the setup we can predict the population of the bound states: The neutrons coming out of the collimator system can be approximately described by plane waves since they occupy only high ex-

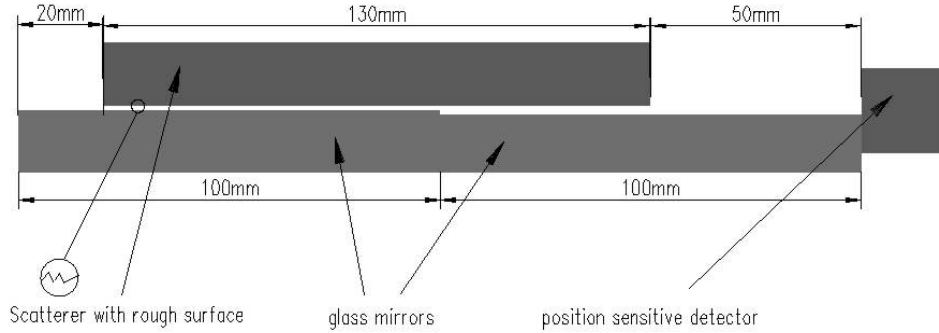


Figure 2.1: Experimental setup for the position measurement performed with a slit of $30\mu m$ between the scatterer and the first mirror and a $21\mu m$ step between the two mirrors.

cited states of the gravitational potential above the floor of the experimental hall. When they reach the mirror they couple into lower gravitationally bound states according to the overlaps between these states and the wave functions describing the "free" neutrons. The time required for this process can be approximated using the energy-time uncertainty relation:

$$\Delta t \approx \frac{\hbar}{\Delta E}, \quad (2.1)$$

where ΔE is the energy of the bound states of the system. For the first few bound states the eigenenergies, classical turning points of the neutron trajectories and the expectation value of z are given in table 1.1. Thus, the time interval for the formation of the ground state is $\Delta t \approx 0.5ms$. The neutrons have a maximum horizontal velocity of about $20m/s$ so it will take them at least $1ms$ to cross the $20mm$ distance between the edge of the first mirror and the scatterer. We conclude that there is enough time for the bound states above the mirror to be populated before the neutrons reach the scatterer. At this point all states are expected to be evenly populated. This is only an approximation since the neutrons would be diffracted at the edge of the mirror so that the population of the ground state would actually be less than that of the other states. The neutrons will be diffracted again at the edge of the scatterer which would again favour the population of the higher states. Unfortunately, the diffraction phenomena inside our mirror-scatterer installation have not been fully explored, yet, but an outline is given in [We01].

Once the neutrons have been transmitted into the space between the scatterer and the mirror, neutrons in the higher states will eventually be removed from the system and only those neutrons in the first three bound

states will be transmitted through the $30\mu m$ slit.

To find out, how the states will be populated after the step between the two mirrors it is necessary to calculate the transition amplitudes from the states above the first mirror to the states above the second mirror, see e.g. [Schw98]. Ignoring the scatterer for a while we can assume the horizontal and vertical states of the neutrons to be independent of each other and consider the eigenstates of the vertical motion only. If we choose $z = 0$ at the top of the second mirror we can see from equation 1.5 that the bound states are:

$$\phi_n^I(\zeta) = A_n Ai(\zeta - \epsilon_n - \sigma_s) \quad (2.2)$$

$$\phi_m^{II}(\zeta) = B_m Ai(\zeta - \epsilon_n), \quad (2.3)$$

$$(2.4)$$

above the first and second mirror, respectively. Here σ_s is the size of the step ($= 21\mu m$) divided by R given in equation 1.3, which is the length scaling factor of the setup. To obtain the transition amplitudes from states above the first mirror onto states above the second one we need to calculate the overlap between these states:

$$T_{nm} \propto \int_0^\infty d\zeta (\phi_n^I(\zeta))^* \phi_m^{II}(\zeta). \quad (2.5)$$

We are assuming that only the first three states above the first mirror and the first five states above the second mirror will be populated. This is due to the approximation that all neutrons with expectation values of z inside the scatterer will be removed from the system whereas all neutrons with expectations values z below the height of the scatterer will be unaffected by it. The population p_n of the n^{th} state above the second mirror will be the sum of the absolute square of the transition amplitudes between this state and the three states above the first mirror:

$$p_n = \sum_{m=1}^3 |T_{mn}|^2. \quad (2.6)$$

The expected relative populations of the states above the second mirror are summarized in table 2.1.

We are assuming that the system is prepared in an incoherent superposition of the eigenstates because the collimator is a highly incoherent neutron source, which has been investigated in [We01]. In this case the density matrix ρ of the system should look like

state number	relative population
1	0.02
2	1.20
3	4.95
4	4.67
5	5.54

Table 2.1: Population of the bound states above the second mirror

$$\rho = \sum_n p_n |\phi_n^{II}\rangle \langle \phi_n^{II}|. \quad (2.7)$$

Now, a measurement of the vertical position z of the neutrons corresponds to a projection of ρ onto the space spanned by the eigenstates of the position operator, $\delta(z - z_0)$, and the probability ω of measuring a certain value z is given by the trace of this projection:

$$\omega(z) = Tr(\rho |z\rangle \langle z|) = \langle z | \rho |z\rangle = \sum_n p_n |\phi_n^{II}(z)|^2. \quad (2.8)$$

This is the fitting function we used in the interpretation of the data with an overall amplitude, the z zero position and the background level as free parameters. To account for the finite resolution of the coated detectors the fitting function has to be convoluted with a Gaussian of half width σ equal to the resolution of the detector. In our calculations we used σ as a free parameter to determine the resolution of the detectors.

The route taken above is the most straightforward way of deriving a prediction for our measurement of the neutron density and is by no means a complete discussion of the phenomena involved. Diffraction, for example, has been ignored completely. Also, the action of the scatterer has not been truly accounted for. We have simply assumed those states with z expectation values below the height of the scatterer to be unaffected by it, whereas all states with higher z expectation values have supposedly been removed completely. It is probably also an oversimplification to assume that at the site of the step, directly beneath the scatterer, the vertical and horizontal motion of the neutrons can be viewed independently of each other. Another tricky aspect of this derivation is the assumption that we are observing an incoherent mixture of states. Yet, we shall see that even with this simplified picture we have arrived at a prediction for our measurement that describes the results quite well.

2.2 Treatment of the data from the position sensitive detector

In summer 2004 two different detectors were used to measure the density distribution of the neutrons. Both of them were nuclear trace detectors made of a special plastic called CR39 ([IC00]) but with different reactive coatings, one was coated with Uranium-235 the other with Boron-10. In this thesis we will deal mostly with the treatment and results from the Boron coated detector (or Boron detector for short) which has been tested during the experimental run of this year. We will only refer to the results of the measurement with the Uranium detector, which has also been used during the experiments performed in 1999 and 2002, for comparison reasons. Detailed information on the preparation, treatment and readout of the Boron detector will be presented in chapter 3.

The Boron detector was installed in the setup discussed in the last section and irradiated for 28 hours. After the irradiation was complete the coating was removed from the trace detector and the plastic was etched in 20% NaOH solution at 45°C for 5 hours to enlarge the nuclear traces. According to our calibration, table 3.4, this corresponds to $(0.45 \pm 0.04)\mu\text{m}$ of the bulk of the detector having been etched off, which is roughly the minimum etch that is necessary to clearly see the traces with a magnification factor of 20. Technically it would also be possible to use lenses with a magnification factor of 50 or 100 which would make the identification of the traces easier as well as allow us to etch away even less of the detector bulk. However, since the automation of the readout procedure is still under development and many things had to be done manually this was not practical. As it was we had to take about 300 pictures of the detector under the microscope which took several hours. With twice the magnification we would have had to take four times as many pictures which can barely be achieved in a day.

The detector is 12cm long, 1.5cm high with a thickness of roughly 1.4mm. Under a microscope a line of photographs was taken of the detector along its long axis at roughly half height. A movable stage was used to move the detector under the microscope. The traces of the α -particles and Li-nuclei produced in the nuclear reaction of neutrons with the Boron nuclei appear as small black circles or disks in the photographs. The coordinates of these circles can be mapped which was done by hand for our detector since our computer programs to identify the traces did not work well enough, yet. Once the data (i.e. the coordinates of the traces) has been read out it has to be corrected for the inclination of the detector under the microscope and

the curvature the detector obtains during the chemical development. This was done in two different ways: Once a marker line of traces was used to fit curvature and inclination (see subsection 2.2.1) and once the width of the signal was minimized, varying the correction parameters by hand. figures 2.2 and 2.3 show the raw data from the Boron detector and a histogram of the z-coordinates of the counted traces.

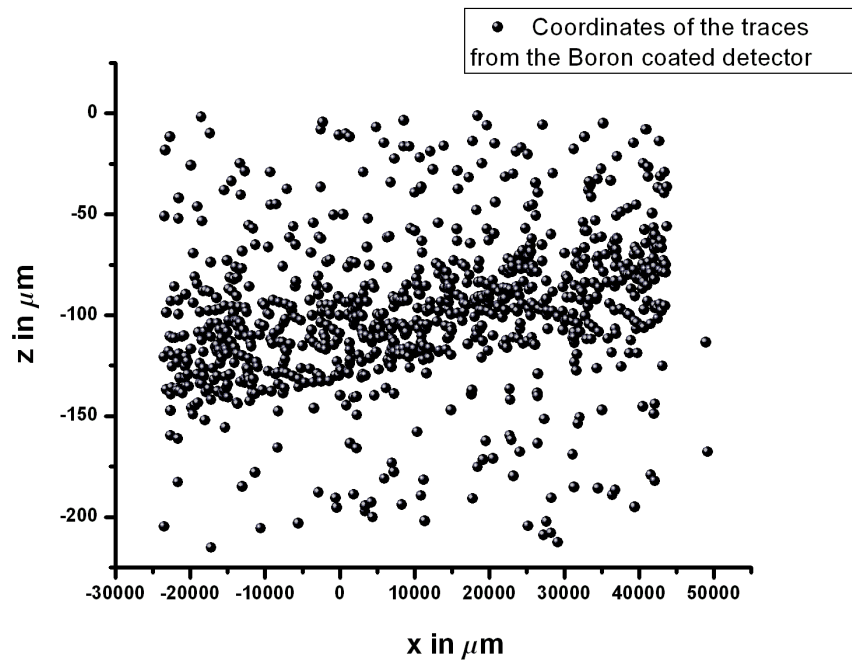


Figure 2.2: Raw data from the Boron detector

2.2.1 Correction of the data using the "edge"

The marker line of traces was produced in the following way: Once the detector had been irradiated in front of the experimental setup, discussed at the beginning of this chapter, it was shifted down by 1mm . Then the slit between the mirrors and the scatterer was increased to $200\mu\text{m}$ and the detector was, again, irradiated for several hours. After the chemical development of the detector the traces from the second irradiation are densely packed in a certain area with a sharp lower edge, where the mirror was. A section of the edge can be seen in figure 2.4. The coordinates of traces from the edge are mapped in the same way as the those of the other traces but we only used part of the information from the edge signature since the

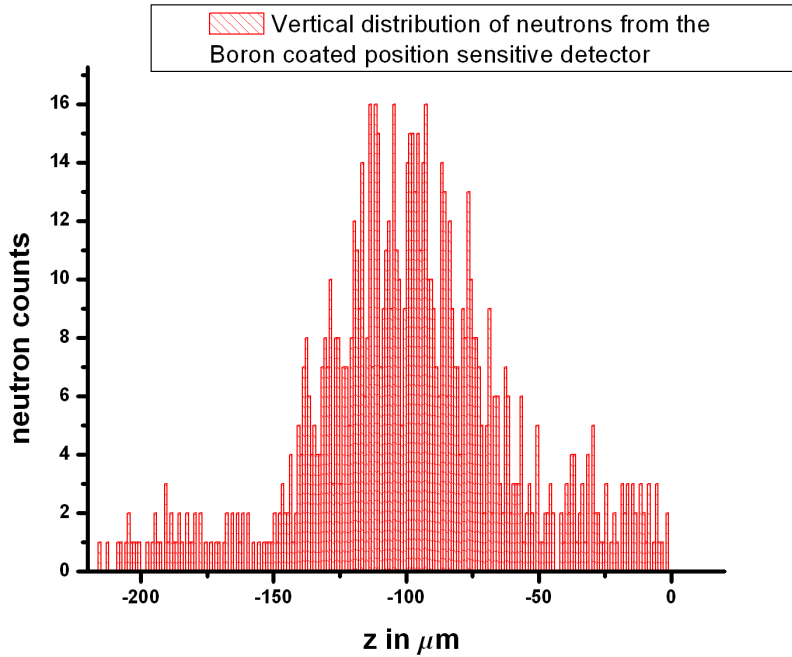


Figure 2.3: Histogram of the raw data

amount of data was simply overwhelming for a standard PC. A picture of the data from the "edge" can be seen in figure 2.5.

The original idea was to do linear and polynomial fits of the edge data and use the obtained values for inclination and curvature to correct the data for the density distribution. This procedure was followed but unfortunately the detector had been shifted under the microscope when it was being photographed. This is also visible in figure 2.2. We can see that the detector has been shifted under the microscope at an x coordinate of about 30mm . This happened because we used a prototype of a movable stage for our microscope which had not been fully developed, yet, and was a little error-prone. Unfortunately, the pictures of the edge had been taken after the shift of the detector so that the inclination of the edge was not comparable to the inclination of the line of data that we are actually interested in.

Figure 2.6 shows the corrected data displayed together with our prediction. The fit function was convoluted with a Gaussian $\sigma = 5.8\mu\text{m}$ which has been fitted to the data and corresponds to the resolution. In figure 2.7 χ_R^2 is shown as a function of σ . The fitted resolution is much worse than what we expected from equation 3.7 which is, of course, due to the

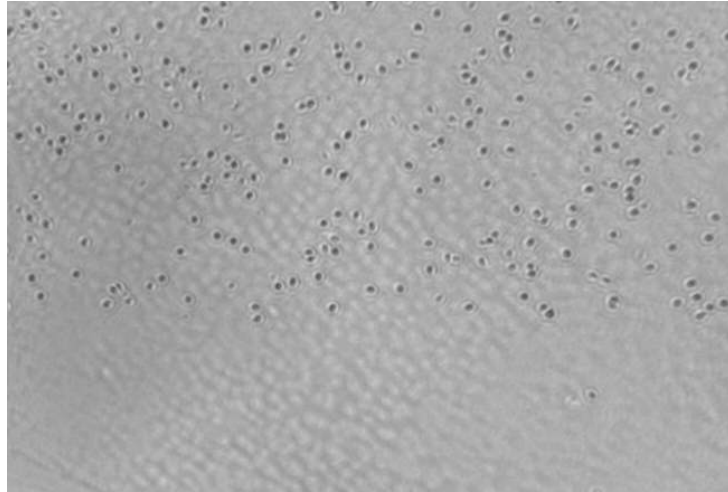


Figure 2.4: Edge of traces for the determination of curvature and inclination of the detector

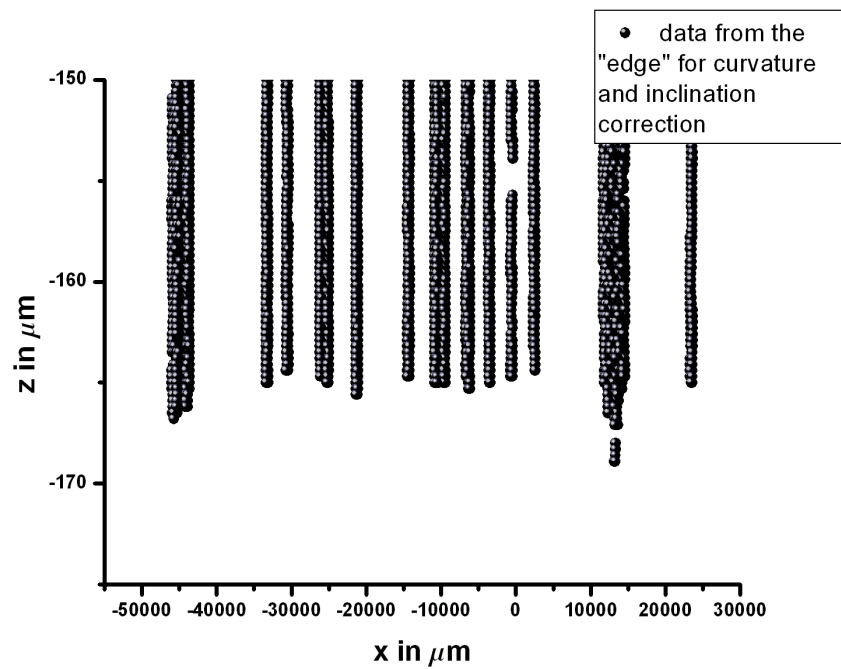


Figure 2.5: A picture of traces from the "edge", the size is approximately $130 \times 90 \mu\text{m}$

inadequacy of the measured inclination.

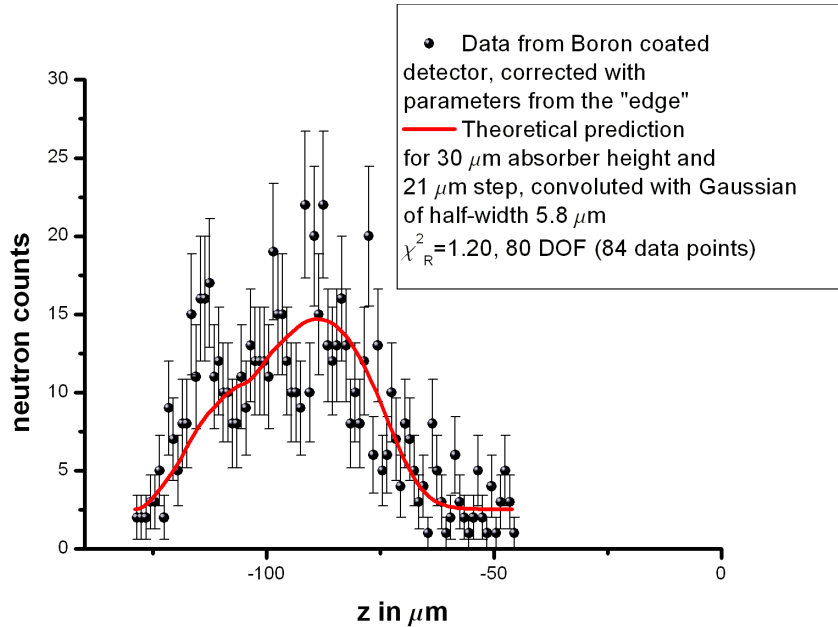


Figure 2.6: Fit of our prediction to the Boron detector data corrected with "edge"-information

2.2.2 Correction of the data by minimizing the width of the distribution

Since we could not use the information from the edge as a means of correction for the inclination and curvature of the detector the correction was performed by minimizing the width of the z -distribution of the data, [Ne04]. The corrected coordinates of the traces are shown in figure 2.8 and the corresponding distribution in figure 2.9. Figures 2.10 and 2.11 show the data together with our theoretical prediction and the determination of the resolution of the Boron detector. The resolution of $1.4\mu m$ is not quite as good as our prediction from equation 3.7 but the predicted value still lies within the 70% confidence region. There are a number of possible reasons for the loss of resolution: firstly, there is quite a high uncertainty in the value of the depth of the etch and, secondly, we did not make a great effort to identify the center of mass of the traces. The quality of the fit, however, is very good and the experimentally determined resolution is also acceptable.

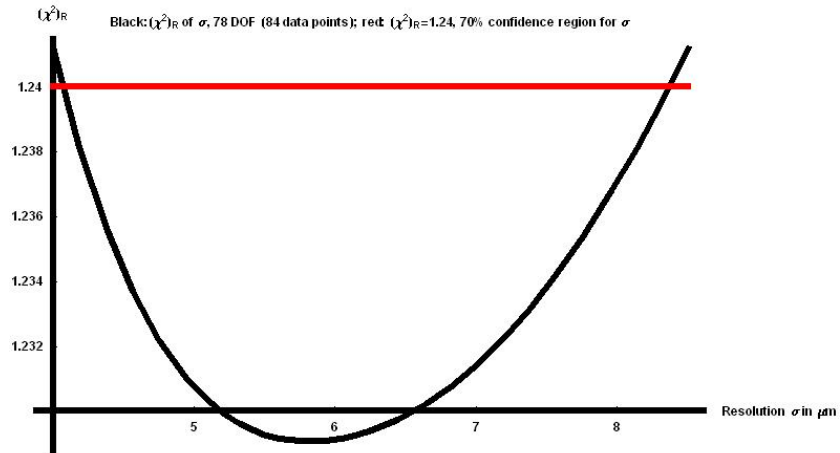


Figure 2.7: Best fit resolution and standard deviation for the Boron detector data corrected with information from the "edge"

The only disadvantage is that we have added two more parameters to our model since curvature and inclination are no longer measured quantities. Therefore it is still be desirable to improve the method of measuring these properties of the data.

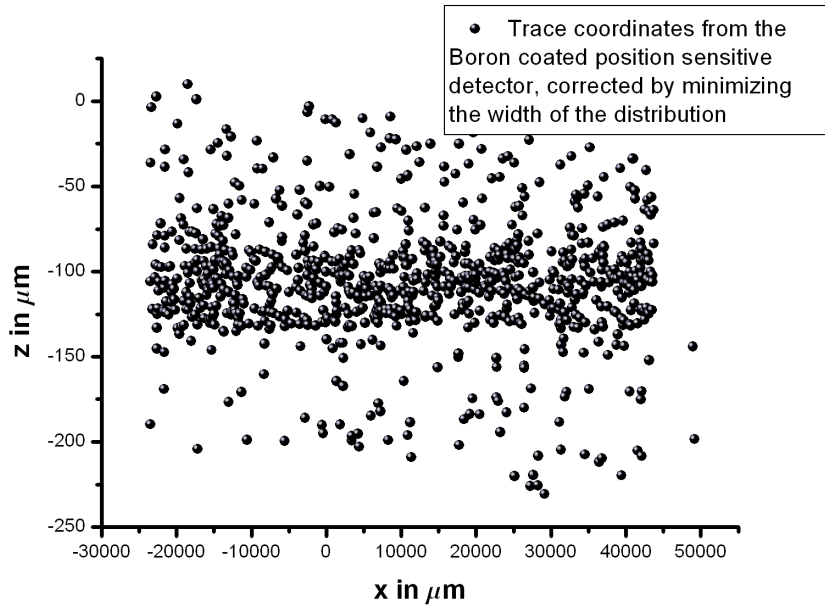


Figure 2.8: Corrected data from the Boron detector

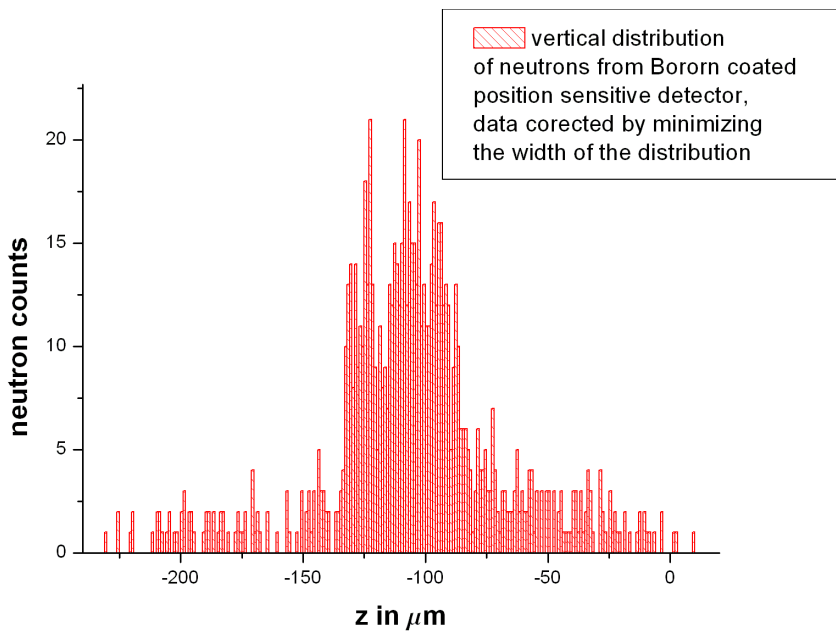


Figure 2.9: Histogram of the corrected data

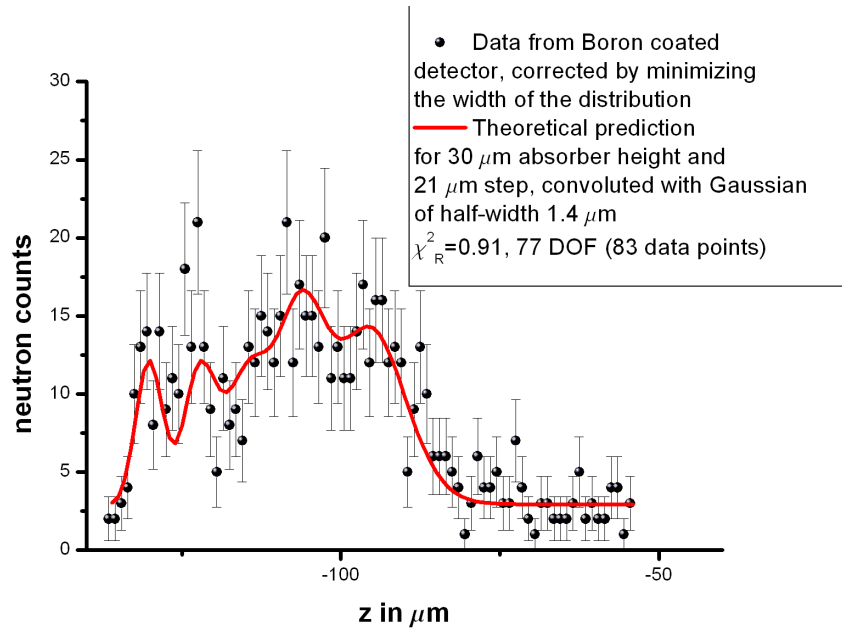


Figure 2.10: Fit of our prediction to the Boron detector data corrected by minimization for the spread of the distribution

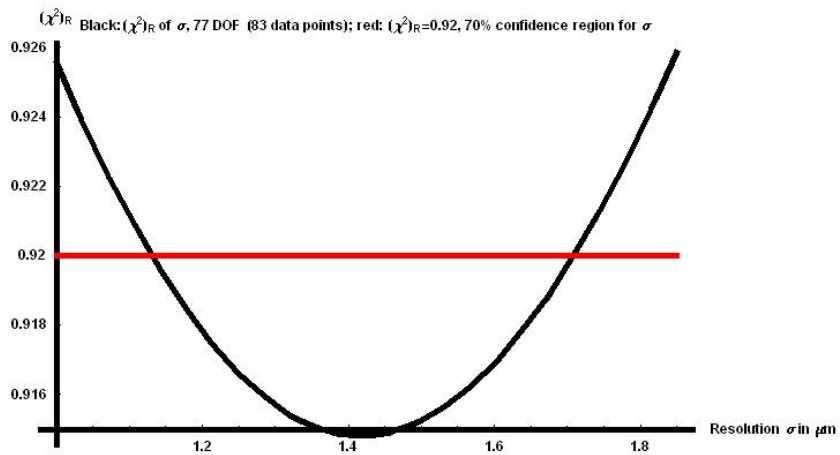


Figure 2.11: Best fit resolution and standard deviation for the Boron detector data corrected by minimizing the spread of the distribution

2.3 Comparison of the Uranium and Boron coated detector

Uranium coated, position sensitive detectors have been used in this experiment before, [Rue00]. The Uranium coating yields an excellent signal/background ratio because there is almost no natural background radiation of the heavy fission products whose traces are to be detected. However, the great disadvantage of this coating is its low efficiency in the detection of neutrons. For this reason, the Boron coated position sensitive detector was put to the test during the experimental cycle of 2004.

Figures 2.12 and 2.13 show χ_R^2 as a function of the resolution of the Uranium detector and our best fit of the Uranium data. These have to be compared with figures 2.11 and 2.10 which show the same curves for the Boron detector. Apparently, we have achieved a better resolution with the Boron detector than with the Uranium detector. This is an unexpected result. It was assumed that the resolution of the Uranium detector would be better, since here the plastic does not have to be etched as far in order to make the traces of the fission products visible. A possible reason for the superior resolution of the Boron detector is that the traces of the Uranium fission products produced in the neutron reaction are up to $20\mu m$ long and appear as thin lines under the microscope. The α - and Li-traces, on the other hand, can hardly be longer than $6\mu m$ and appear as small dots or craters. This makes it much easier to identify the tip of the trace and may counter the effect of the required larger etching process. Additionally, the maximum angle under which the traces of the fission products can be detected may be higher for the Uranium detector. This would also result in a loss of resolution (see section 3.5). Unfortunately, the critical detection angle has, at this point, only been calculated for the Boron detector.

A comparison of the data to our predicted distribution function also yields a better fit for the Boron detector, due to better statistics. However, the two datasets from the two different detectors show the same, quantum mechanical, tendency: a first peak in the distribution and afterwards a significant minimum followed by a second, much broader maximum. This tendency is also a clear feature of our quantum mechanical prediction.

A combination of the data from the Boron and Uranium detectors is displayed in figure 2.14. The resolution of the final data can be deduced from 2.15. Although statistics are much better for this dataset the fit is not as good as that of the Boron detector data alone.

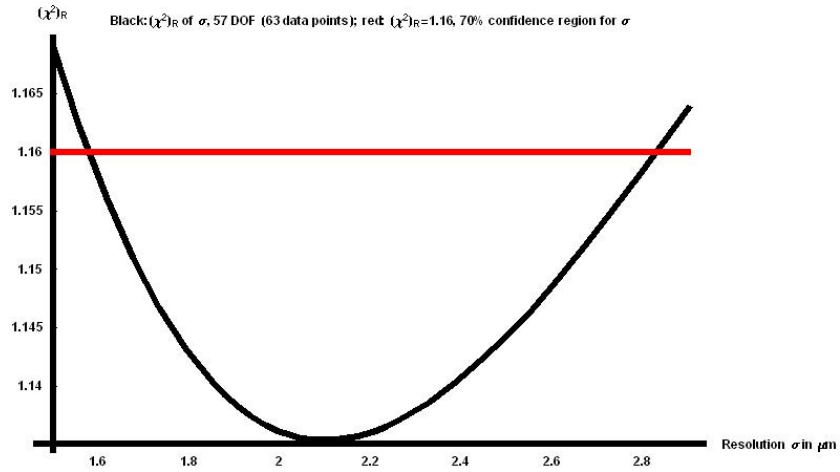


Figure 2.12: Best fit resolution and standard deviation from the Uranium detector data

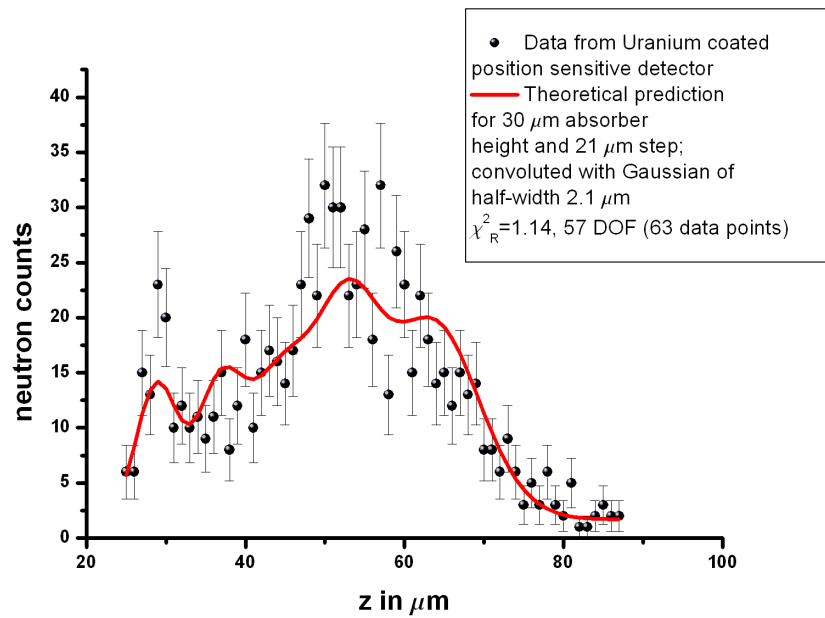


Figure 2.13: The theoretical prediction for transmission together with the data from the Uranium coated detector

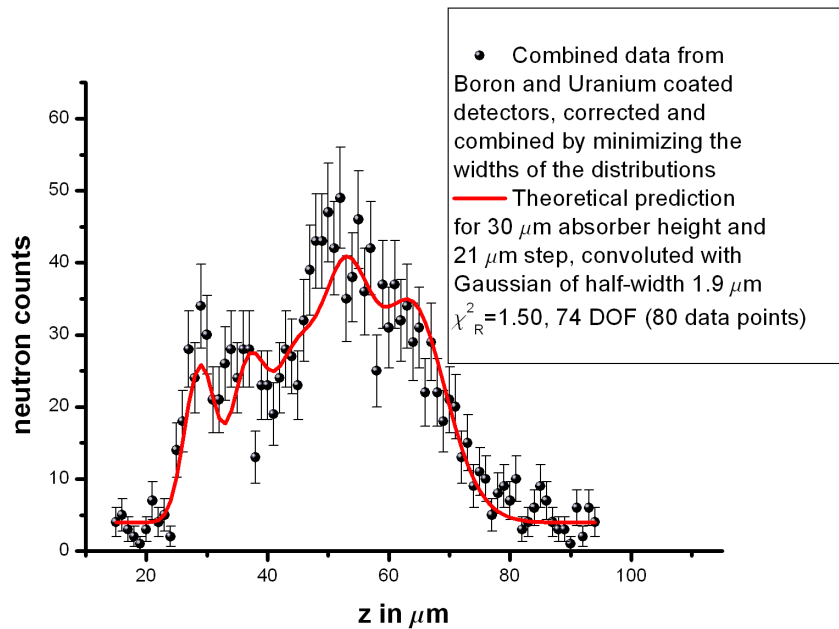


Figure 2.14: Fit to the combined data from Boron and Uranium detector

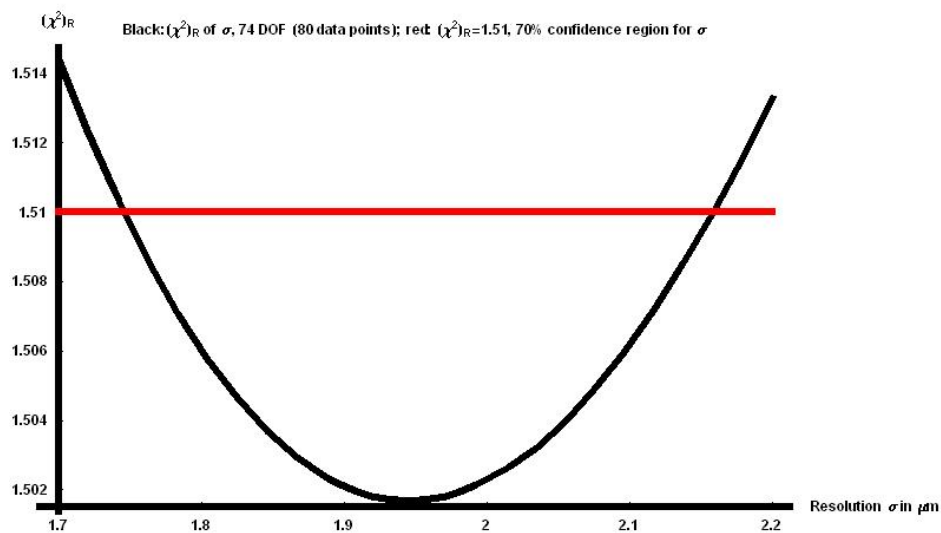


Figure 2.15: Resolution of the combined data

2.4 Classical versus quantum mechanical interpretation of the measurement

The most significant and far reaching question concerning the measurement of the neutron density distribution above the mirror is whether or not we have identified a quantum mechanical phenomenon. Unfortunately, the answer is only "maybe", for now.

The classical prediction for the density distribution of the neutrons can not be calculated analytically because of the large step between the two mirrors. We therefore used Monte Carlo simulations to gain an insight into the classical behaviour of the system, [We01]. In this simulation the trajectories of classical particles through the scatterer-mirror system are calculated. The initial velocities of the particles follow a Boltzman distribution. If we look at the classical prediction for the density distribution shown in figure 2.16, which was computed using a Monte Carlo simulation with 10^9 iterations, we can see that the qualitative behaviour of the function is different from our quantum mechanical description.

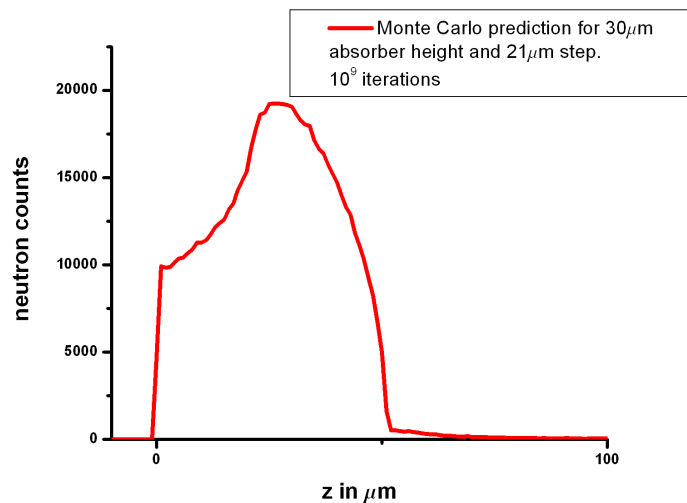


Figure 2.16: Result of a Monte Carlo simulation for the classical prediction of the neutron density

Due to the bad statistics of the data the Monte Carlo prediction still yields an acceptable fit to both the data obtained from the Uranium and Boron detectors which can be seen from figures 2.17 and 2.18. The fit of the Monte Carlo prediction to the combined data from both detectors is

even better than the fit of the quantum mechanical expectation, which can be seen from figure 2.19.

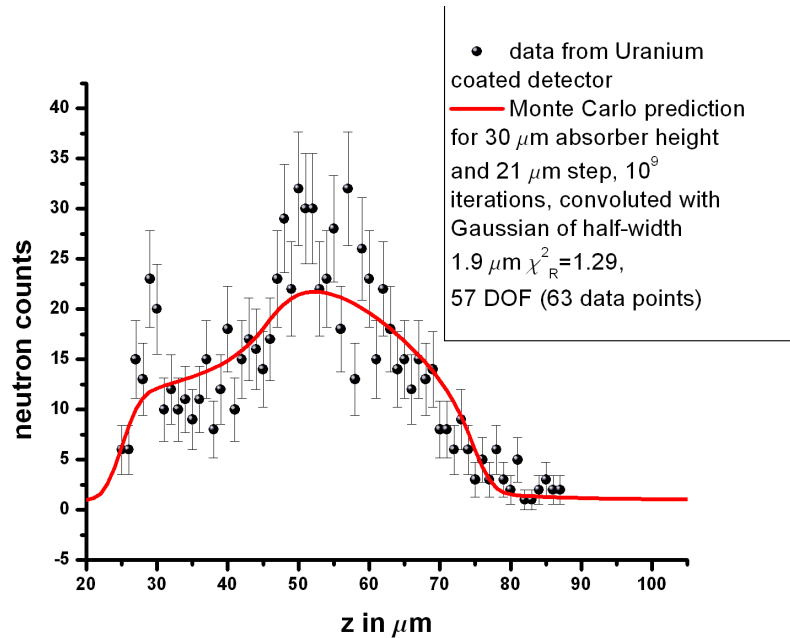


Figure 2.17: Fit of the Monte Carlo prediction to the data from the Uranium detector

If we use Monte Carlo simulations which yield statistics similar to those of the actual measurements we observe effects of classical statistics which can be very similar to the quantum mechanical expectation. This is shown in figures 2.20 and 2.21. The two fitting functions were obtained from two different runs of our Monte Carlo simulation and fitted to the data with the same free parameters as the quantum mechanical function. The classical curve in figure 2.20 describes the Boron detector data very well and it even shows the same qualitative behaviour. The classical curve in figure 2.21, on the other hand, is qualitatively quite different from the data but also yields an acceptable fit due to the bad statistics of the measurement.

Figure 2.22 shows a fit of the sum of the two Monte Carlo simulations to the combined data. This function requires a rather unrealistic value for the half-width of the convolution Gaussian which is smaller than our theoretical prediction (see equation 3.7). This was also the case for the fit of the high-statistics Monte-Carlo simulation to the combined datasets.

Although the quantum mechanical prediction yields better results for

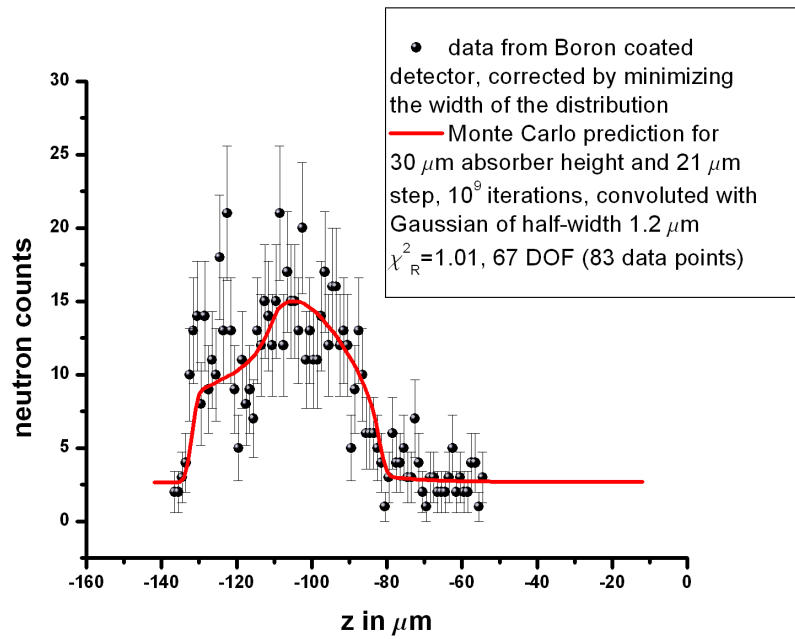


Figure 2.18: Fit of the Monte Carlo prediction to the data from the Boron detector

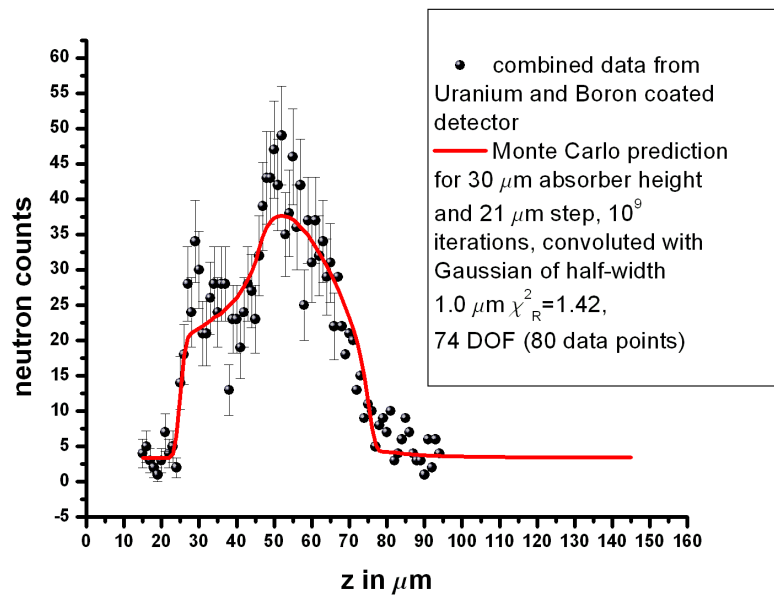


Figure 2.19: Fit of the Monte Carlo prediction to the combined data of the Boron and Uranium detectors

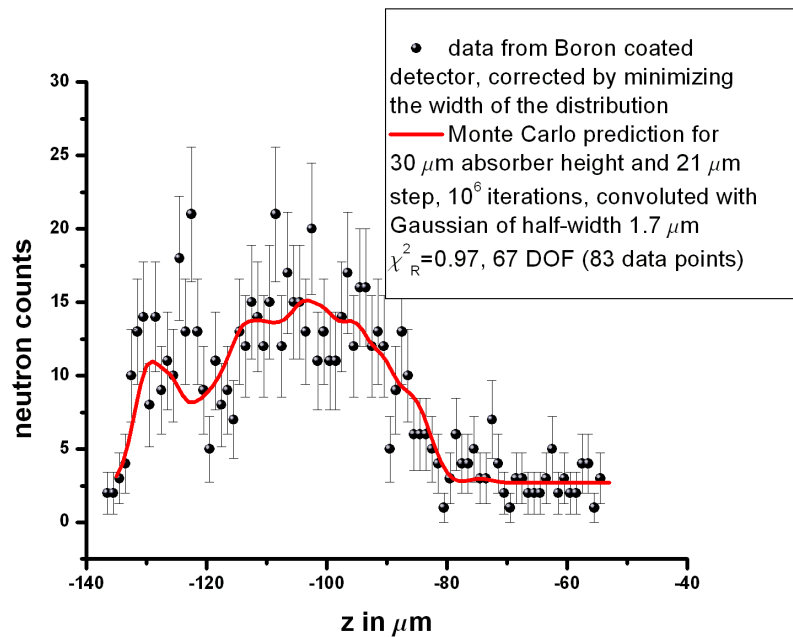


Figure 2.20: Fit of a classical Monte Carlo simulation to data obtained from the Boron detector

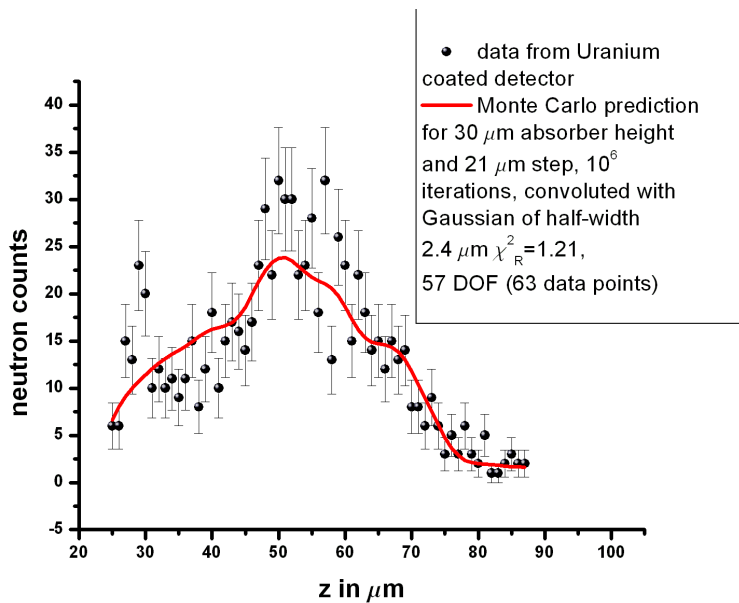


Figure 2.21: Fit of a classical Monte Carlo simulation to data obtained from the Uranium detector

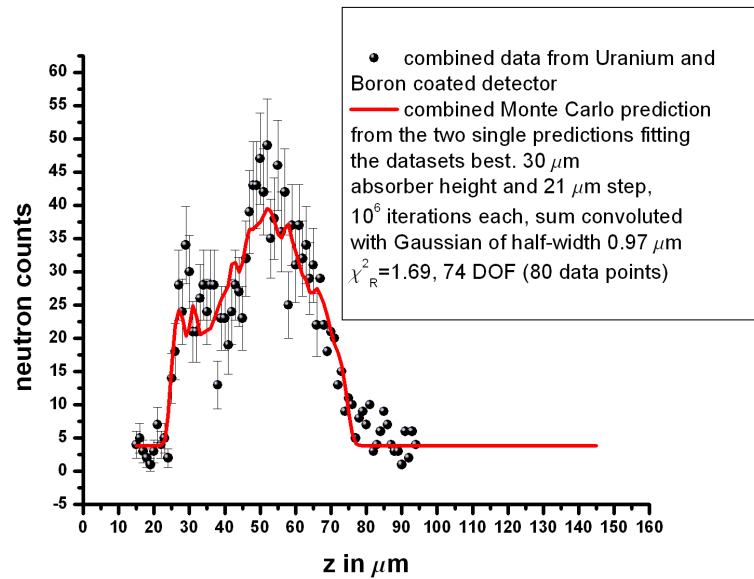


Figure 2.22: The sum of the Monte Carlo distributions shown in figures 2.20 and 2.21 are fitted to the combined data of the Boron and Uranium detector

both the Boron and Uranium detector data, we can not exclude the classical case, not even with a probability of 50%. For the combined data of the two detectors the classical prediction even yields the better result although the value for the resolution in this fit is not realistic. To clearly distinguish between the two models it is necessary to greatly improve the statistics of the measurement which will be done during the next experimental cycle, February 2005.

Chapter 3

The Boron coated, position sensitive detector

To perform a measurement of the distribution of the neutrons once they have passed the waveguide it is essential to have a neutron detector with a high spatial resolution below. It is possible to achieve such a high resolution of $1 - 2\mu m$ with a nuclear trace detector coated with a target material that will undergo a nuclear reaction with an incoming neutron. The fission products of this reaction then leave traces in the trace detector that can be reconstructed under a microscope after some chemical treatment.

In this chapter the preparation and function of position sensitive neutron detectors with a ^{10}B coating is described. The nuclei in the Boron layer undergo a nuclear reaction with an incoming neutron producing a Li-nucleus and an *alpha*-particle. One of the two will be transmitted into the plastic and leave a trace there. During the experimental run of 2004 such detectors were tested and the results are discussed in chapter 2. The idea of using a Boron-10 coating for this task came from the CASCADE detector group, [Klei01].

For a short "recipe" for the preparation, coating, development, read-out and general treatment of the detectors see appendix A.

3.1 The uncoated CR39 trace detectors

There are many materials, e.g. plain glass or many of the readily available solid polymers, that could potentially be used as nuclear trace detectors. The plastic we use is called CR39 and is manufactured especially for use as nuclear trace detectors (and sunglass lenses) by Intercast Europe S.p.A. [IC00]. This plastic has superior chemical and physical properties and it

also has the advantage that all of these properties have been thoroughly tested by many different research groups (e.g. [Cec01]).

The CR39 plastic is made from dietilenglycolbisallylcarbonate (ADC) by polymerization. This monomer has two of its allyl functional groups and because of this it is cross-linked as well as polymerized which results in a thermosetting plastic that is hard and insoluble in most solvents. A summary of some of its properties is shown in table 3.1, [IC00].

Specific Weight at 25°C	1.32g/cm ³
Rockwell Hardness	M95-M100
Maximum Temperature Recommended continuous service	100°C
one time, one hour duration	130°C

Table 3.1: Properties of CR39

These properties are important for the use of the CR39 plastic in our experiment. During the application of the Boron-/Uranium-layer and during the chemical treatment after irradiation the plastic can get quite hot and it is, of course, crucial that it will not start to melt away or significantly change its shape. The CR39 is mostly only elastically deformed during these processes and will come back to its original shape after slow cooling. Sometimes the detectors are bend a little after the final chemical treatment but this curvature can be measured and corrected for in the analysis of the data, as was discussed in chapter 2.

The hardness of the plastic is also very fortunate for us. Small defects and scratches in the surface can sometimes either be very similar to the nuclear traces we are looking for or they could block the view of the traces because a trace will not be visible on top of another, bigger defect in the plastic. If the plastic is handled carefully its surface will normally not show too many defects and scratches due to the hardness of the polymer.

The CR39 trace detectors work in the following way: When a charged particle, an α -particle or Li-nucleus for the Boron coated detector, passes through the plastic it will damage some of the bonds of the polymers. This damage can be increased by chemical etching so that it eventually becomes visible under a standard optical microscope. After the treatment the particle traces can look like small holes, cones or even long, thin lines as is the case for the traces from the Uranium coated detectors. Figure 3.1 shows some typical α -traces. The way the traces appear depends, of course, on the extent of the chemical etching but also on the energy and charge of the particle that left the trace.

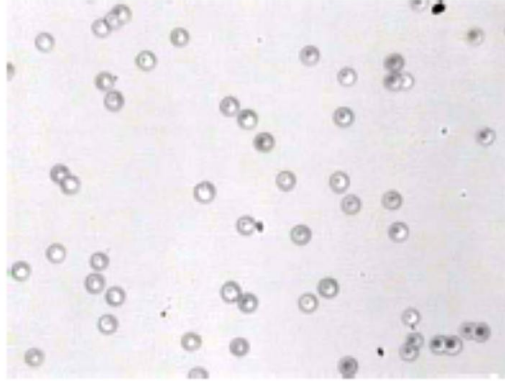


Figure 3.1: α -traces in CR39

Ageing and fading effects of the plastic are small ([Cec01]), i.e. the response of the plastic does not change greatly over time and is only influenced very little by the time passing between the exposure and the chemical treatment of the plastic. There are also some variations in the reduced etch ratio from one production batch to another and we have indications that the density of the plastic is not completely uniform so that p may even vary for different regions of the same detector, [Luk041]. All these effects are smaller or have the same order of magnitude as the uncertainty of the bulk etch velocity v_b . They therefore do not limit our experimental accuracy at the moment.

3.2 Identification of the traces in the CR39 detector

The response of the detector to particles of different charge and energy is measured by the so-called reduced etch ratio p ,

$$p = v_t/v_b, \quad (3.1)$$

where v_t is the track etch velocity and v_b the bulk etch velocity. p is a function of the restricted energy loss of the particles. The restricted energy loss of a charged particle in a certain material is calculated using the Bethe-Bloch formula with an energy cutoff of several hundred eV and it is proportional to $(Z/\beta)^2$, [Flei75]. Figure 3.2 shows a calibration curve of the reduced etch ratio p as a function of the restricted energy loss for several different production batches of the CR39, copied from [Cec01].

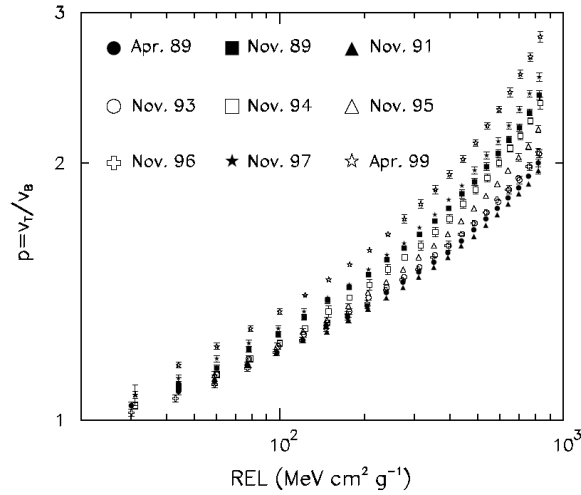


Figure 3.2: Calibration of p vs. restricted energy loss for several CR39 production batches, [Cec01]

The diameter D of the base of a trace after a certain etching time t depends on p and therefore also on the restricted energy loss. The relation between D and p for normally incident particles is ([Flei75])

$$p = \frac{1 + \left(\frac{D}{2v_b t}\right)^2}{1 - \left(\frac{D}{2v_b t}\right)^2}. \quad (3.2)$$

It is therefore possible to identify a particle by the size of its etch pit base. This fact can be used to reduce the background since only traces of a certain diameter have to be taken into account. The α -particles and Li-ions produced in the Boron layer have an initial energy of 1.47MeV and 0.83MeV , respectively, see table 3.5. For these initial energies the energy loss dE/dx and maximum range R_{max} of the particles in solid Boron was calculated. The result is shown in table 3.2. From the maximum range and the energy loss the minimum energy of particles reaching the CR39 layer can be calculated. The maximum energy is equal to the initial energy for particles being produced directly at the edge of the CR39. The range of α -particles and Li-ions of these energies in the CR39 layer are shown in figures 3.3 and 3.4 and their energy loss in the CR39 is shown in figures 3.5 and 3.6. These curves were calculated using SRIM [SRIM]

For the detector we used in the measurement of the density distribution of the neutrons discussed in chapter 2 the depth of the etch was

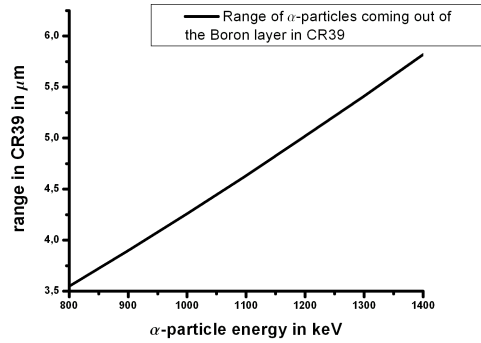


Figure 3.3: Range in CR39 of α -particles produced in the Boron layer

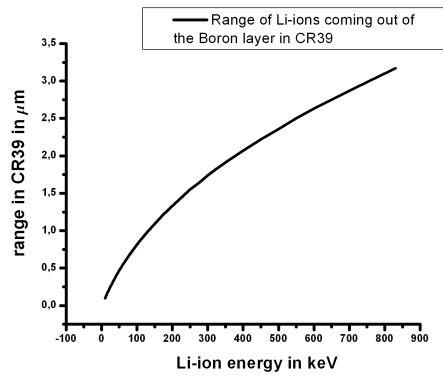


Figure 3.4: Range in CR39 of Li-ions produced in the Boron layer

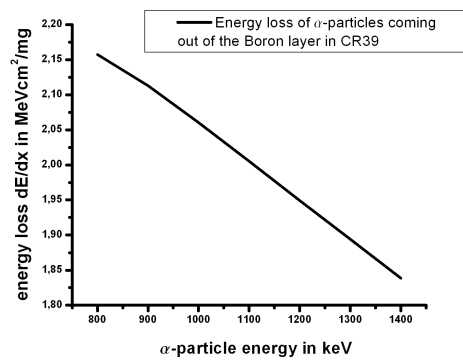


Figure 3.5: Energy loss dE/dx in CR39 of α -particles produced in the Boron layer

particle	dE/dx in $\text{MeV cm}^2/\text{mg}$	R_{max} in μm
α	1.638	3.53
Li	3.159	1.82

Table 3.2: Energy loss and maximum range of the produced Li-ions and α -particles in Boron

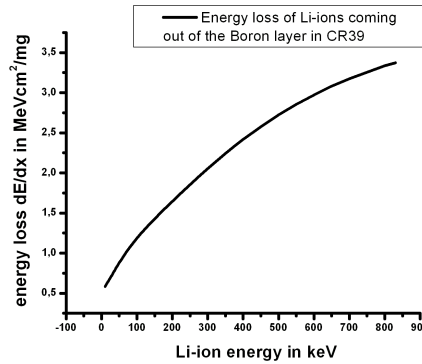


Figure 3.6: Energy loss dE/dx in CR39 of Li-ions produced in the Boron layer

roughly $0.5\mu\text{m}$ and the average trace diameter was $1.5\mu\text{m}$. These values correspond well to what we would expect for particles with that energy loss from figure 3.2.

3.3 The application of the ^{10}B coating

The ^{10}B coatings were applied in an evaporation device where an electron beam is used to evaporate the Boron and the substrate could not be heated. The detectors are attached to a slowly circling substrate holder, 50 cm above the source. Because the substrate holder is circling above the Boron source the atoms will seem to spread as a spherical wave. The detectors are fastened to the holder tangential to the Boron cloud to get maximum uniform coating, [Rue00]

Usually, Aluminium holders were used to fasten the detectors to the substrate holder. We have now started to use plastic 'clips' for two reasons: Firstly, the plastic is comparatively softer than the metal and will not scratch the surface of the detectors. Secondly, the plastic 'clips' are thermal insulators so that there won't be a great heat transfer from the detectors to the substrate holder, thus the surface temperature of the plastic

will be higher during the coating process. This is supposed to improve the quality of the Boron layer since the atoms will not cool down as quickly but move around on the surface more, therefore arranging themselves in a more uniform lattice with better cohesion to the plastic surface.

Boron is a ceramic material and not very flexible. When it is coated onto an elastic material such as our CR39 the layer will get cracks very easily. It is therefore important to let the detectors cool down very slowly after the coating process so as to ensure that there are no rapid changes in the shape of the CR39. Afterwards the detectors have to be handled with great care.

Applying thin films to a surface often seems to be more art than science, or possibly alchemy. Everybody has their own, secret recipe of how to achieve the best results, but in any case it seems to be very important how the substrate is treated before the coating is applied. We used a series of ultrasonic baths of Benzinum (a non polar solvent), followed by Iso-propanol (a polar solvent) and demineralised water, sometimes aided by cotton-wool-rubbing, see appendix A for details. This was done to ensure that all kinds of pollutants, both non polar and polar, would be removed. If the surface is not cleaned thoroughly the coating will usually have many defects where water can get in between the Boron layer and the plastic. Since Boron is slightly soluble in water this will eventually cause the coating to peel off.

Our success rate with the coating of our detectors was devastating. Out of 62 coated detectors only 7 ended up having a nice, even, scratch-free coating. There were a number of problems: Firstly, the detectors were polluted with some kind of grease which could not be washed away with alcohol or acetone which is what we had been using to clean up to then. When the plastic is not cleaned properly the coatings are very unstable and can easily get scratches into them. Another problem was that we had overestimated the vacuum inside the evaporation device. This meant that the Boron could react with Nitrogen inside the device forming a layer of Boron Nitride instead of pure Boron crystals.

Some of the coatings looked quite well at first but started to deteriorate after very quickly after the detectors were taken out of the evaporation device. In these cases the coatings probably at small defects at the beginning and were then dissolved by atmospheric water. Even if the coatings are homogeneous and scratch-free at first it is always advisable to store the coated detectors in a very dry environment.

3.4 The treatment of the irradiated detectors

The chemical treatment needed to enable a readout of the detectors under a standard optical microscope consist of, firstly, removing the reactive coating from the trace detector and, secondly, etching the detector to increase the size of the traces. This etching which is in our case performed with 20% NaOH solution is one of the crucial steps in the treatment of these high-resolution detectors because it ultimately limits the spatial resolution: When the traces are etched out the bulk of the detector is also being etched away which means that the point of impact of the trace, seen later under a microscope, is not the real point of impact of a fission product on the plastic surface (let alone the point of impact of the neutron on the coating) but some point along the trace of the particle through the plastic, see figure 3.7. However, if the traces are not sufficiently enlarged they become difficult to distinguish from defects in the plastic and the signal/background relation gets worse. It is therefore essential to optimize the visibility and potential spatial resolution when etching the detectors.

Since Boron is slightly soluble in water it usually suffices to immerse the coated detector into a water bath and heat it up slowly to remove the coating. If this doesn't work the detector can be washed with hydrochloric acid which will react with the Boron but leave the plastic intact. In any case, the Boron will also react with the Sodium ions in the NaOH solution to form Borax salt which would remove any remaining Boron atoms from the plastic surface without measurably influencing the etching process.

The bulk etch velocity v_b depends on the density of the plastic, the concentration of the etchant and, most importantly (i.e. exponentially), on the temperature of the etching solution, see table 3.3 copied from [IC01]. Normally, a fast etching process would seem desirable since the etching conditions can be controlled more easily over a short period of time. On the other hand, small variations in temperature at low temperatures will only have a small effect on v_b whereas, at high temperatures, there would be a drastic changes in the etch rate even for small variations in temperature. Additionally, the higher the temperature of the etching solution, the greater is the risk of nonelastic deformation of the plastic leading to a curvature of the detector surface which has to be corrected for during the analysis of the data and will worsen the resolution of the detector. We therefore settled on etching our detectors at 45°C where $v_b \approx 0.1\mu m/h$. To decrease nonelastic deformation further the detectors were first put into a water bath at room temperature and slowly warmed up to 45°C.

Since no production batch of CR39 is exactly the same as another it

Temperature ($^{\circ}C$)	bulk etch velocity ($\mu\text{m}/\text{h}$)
40	0.100 ± 0.002
70	1.20 ± 0.02
80	4.20 ± 0.21

Table 3.3: Reference etch rates given by Intercast Europe, [IC01]

is necessary to recalibrate the bulk etching velocity for every new set of detectors. For our detectors this was done by measuring the decrease in weight of a detector after it had been emerged in the etching solution for nearly two days, see 3.4. The result is that $v_b = 0.09 \pm 0.02 \mu\text{m}/\text{h}$ at an average temperature of 45°C .

Temperature ($^{\circ}C$)	bulk etch velocity ($\mu\text{m}/\text{h}$)
45	0.09 ± 0.02
60	0.4 ± 0.14

Table 3.4: Etch rates we measured for our detectors

The change in weight has to be measured very carefully because the weight of a given piece of the polymer changes with atmospheric conditions. This is due to the deposition of water on the plastic surface. Therefore, all weights have to be measured in equilibrium with constant atmospheric conditions (i.e. in a closed box). The reason that the quality of our measurement was not as good as that of the Intercast calibrations was our unsophisticated equipment at the time which made it impossible to properly control the temperature of the etchant. Controlling the etch rates is vital for obtaining the best possible resolution with the detectors and every unnecessarily removed nm of the bulk is an inconvenience.

3.5 The resolution of the detector

The amount of the bulk of the detector that is etched away will ultimately limit the spatial resolution of the detector, as is illustrated in figure 3.7. The resolution is given by,

$$\sigma = r \cdot \tan \theta, \quad (3.3)$$

where $r = d_B + d_e$ with d_B , the distance in Boron that the fission particle has to overcome for $\theta = 0$ (this distance is maximally equal to $0.2 \mu\text{m}$ if the neutron reaction takes place directly at the outward surface of the Boron

coating) and d_e , the depth of the etch of $0.45\mu m$. The maximum angle θ_c under which the traces will be visible is about 81° (see section 3.6).

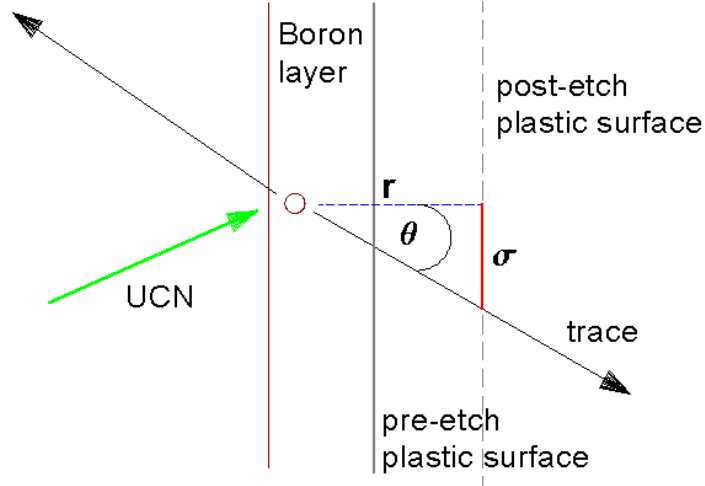


Figure 3.7: Illustration of the limited resolution of the detector

To calculate the resolution of the detector it is necessary to account for the possible angles of the traces in the plastic and for the different reaction sites inside the Boron layer. The differential probability $p_a(\theta)$ of finding a trace with an impact angle θ is simply

$$p_a(\theta) = \frac{1}{\sin \theta}. \quad (3.4)$$

The propability $p_{abs}(x)$ of a neutron reaction taking place at a depth x inside the Boron layer is

$$p_{abs}(x) = \frac{N_A \rho}{A} \sigma \exp\left(-\frac{N_A \rho}{A} \sigma x\right), \quad (3.5)$$

where N_A is Avogadro's constant, ρ is the density of the target material and σ its absorption cross section. For ^{10}B $\rho = 2.16\text{g}/\text{cm}^3$ and for thermal neutrons, $v = 2224\text{m}/\text{s}$, the absorption cross section σ of ^{10}B is $4.01 \cdot 10^3\text{barn}$. σ depends inversely on the velocity of the neutrons:

$$\sigma(v) = \sigma_0(v) \frac{v_0}{v}. \quad (3.6)$$

The neutrons passing through our experimental installation have an average velocity of $5\text{m}/\text{s}$. Thus, for these neutrons, $\sigma = 1.78 \cdot 10^6\text{barn}$.

It is now possible to integrate over all possible angles and reaction coordinates inside the Boron layer to calculate the total resolution σ_{tot} of the detector:

$$\sigma_{tot} = \int_{x=0}^{x_{max}} dx \cdot p_{abs}(x)r(x) \int_{\theta=0}^{\theta_c} d\theta \cdot p_a(\theta) \tan \theta = 1.2\mu m, \quad (3.7)$$

where x_{max} is the thickness of the Boron layer and, in our case, equal to 200nm. The value predicted for the resolution corresponds very well to the resolution we measured (see subsection 2.2.2 and especially figure 2.10). The actual resolution of $1.4\mu m$ is a little worse than the predicted one which is most probably an effect of the manual readout-procedure.

3.6 Detection principle and efficiency

In former runs of this experiments the CR39 trace detectors were coated with Uranium Tetrafluoride UF_4 . The Uranium nuclei undergo nuclear reactions with the neutrons producing two heavy fission products one of which will go into the plastic and leave a trace there. In the experimental run summer 2004 we also used a Boron-10 coating for the CR39 detectors. The ^{10}B nuclei undergo a nuclear reaction with the incoming neutrons producing Li nuclei and α -particles which leave traces in the plastic, see Figure 3.8.

There are two possible channels for this reaction which are listed in table 3.5.

probability	reaction	energy	particle	energy
93%	$n(^{10}B, \alpha)^7Li$	$+2.3MeV + \gamma(0.48MeV)$	α	$1.47MeV$
			7Li	$0.83MeV$
7%	$n(^{10}B, \alpha)^7Li$	$+2.79MeV$	α	$1.77MeV$
			7Li	$1.01MeV$

Table 3.5: Nuclear reaction of ^{10}B with neutrons

This coating has the main advantage that ^{10}B has a much higher absorption cross section for neutrons than Uranium so that a layer of the same thickness will be much more efficient. This helps to increase the overall efficiency of the detector since it is not possible to achieve stable UF_4 coatings of arbitrary thickness.

The efficiency of the detector is determined by the probability of a neutron reaction within the coating and the detection efficiency of the trace

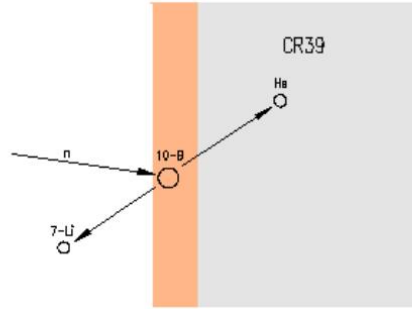


Figure 3.8: Schematic drawing of the boron coated detector

detector. The efficiency of the coating depends on the absorption cross section of the material and the thickness in the following way:

$$P = 1 - e^{-\frac{N_A \rho}{A} \sigma d}, \quad (3.8)$$

where P is the probability of a neutron reaction, N_A is Avogadro's constant, ρ is the density of the target material, d its thickness and σ its absorption cross section. For ^{10}B $\rho = 2.16\text{g/cm}^3$ and for thermal neutrons, $v = 2224\text{m/s}$, the absorption cross section σ of ^{10}B is $4.01 \cdot 10^3\text{barn}$. σ depends inversely on the velocity of the neutrons:

$$\sigma(v) = \sigma_0(v) \frac{v_0}{v} \quad (3.9)$$

The neutrons passing through our experimental installation have an average velocity of 5m/s . Thus, for these neutrons, $\sigma = 1.78 \cdot 10^6\text{barn}$ and for a coating of $d = 200\text{nm}$ thickness, which was used in the experiment, we have a probability of 99% for a neutron reaction in the Boron layer.

The main factor limiting the efficiency of the nuclear trace detector is the existence of a critical detection angle which is illustrated in figures 3.9 and 3.10. The trace shown in figure 3.9 can not be etched because the bulk of the plastic is being removed at a faster rate than the normal component of the trace etch velocity v_t . The trace shown in figure 3.10 has been left by

a particle entering the detector exactly at the critical angle Θ_c above which traces can be registered ([Flei75]).

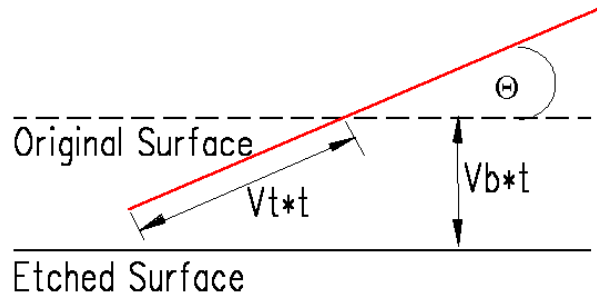


Figure 3.9: Unetchable trace with entrance angle below the critical angle of detection

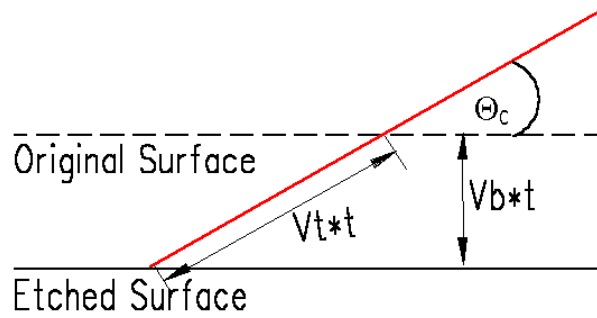


Figure 3.10: Trace of a particle entering the plastic at the critical angle

The critical angle is given by the formula,

$$\Theta_c = \arcsin\left(\frac{v_b}{v_t}\right), \quad (3.10)$$

where v_b and v_t are the bulk and trace etch velocity as before. In the last section we have seen that the reduced etch ration $p = v_t/v_b \approx 3$ for our detectors. The critical angle of entrance for the α -particles and Li-ions produced in the Boron layer is therefore $\theta_C \approx 19^\circ$. The efficiency ϵ of the trace detector is then given by

$$\epsilon = 1 - \sin(\theta_C) \approx 67\%, \quad (3.11)$$

which is just the detectable part of the surface of the half sphere described by the traces. The overall efficiency of the Boron detector is the product of the efficiency of the coating and the detection efficiency of the trace detector. For the neutrons in our installation this efficiency is 66%.

We tested the efficiency of our Boron detectors at the UCN test beam at ILL. First, the flux was measured using a Helium detector, then several detectors were irradiated for a certain period of time. The efficiency we measured was 50% for the test beam neutrons. The velocity spectrum of these neutrons is shown in figure 3.11, [Schmi04]. From equations 3.8 and 3.9 the efficiency P of the Boron coating can be calculated and $P = 80\%$. Together with the efficiency of the trace detector this yields an overall detection efficiency of 54%, comparable to the result of the efficiency measurement.

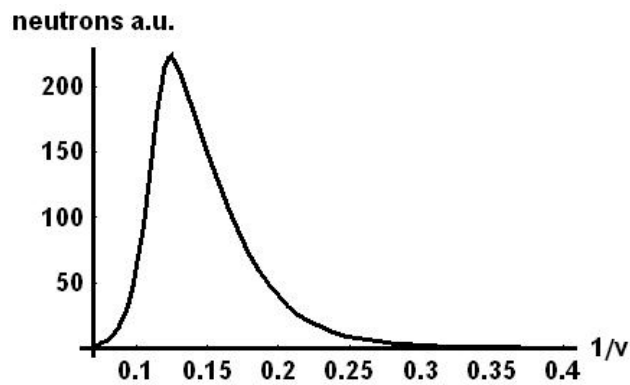


Figure 3.11: Velocity spectrum of the test beam at ILL

The prediction can even be improved if the surface roughness of the plastic detector is taken into account: If the surface is assumed to be totally flat neutrons that cross the Boron layer without being absorbed would be reflected from the plastic surface back into the Boron layer where they would then finally be absorbed. If the surface is assumed to have a roughness of, say, $100nm$ the neutrons would see the potential of the surface smeared by an error function of half width $\sigma = 100nm$ (this is the same argument that we used for the model of the scatterer in chapter 1). Some of the neutrons would then not be reflected back into the Boron layer. Instead they would be absorbed by the plastic detector itself. If this effect is calculated for a roughness of $100nm$ the efficiency of the Boron layer for the test beam neutron spectrum is 75% so that the overall detection efficiency is then 50%, exactly as measured.

3.7 Background

The main disadvantage of the Boron coated detectors compared to those with a Uranium coating is that the background on the Boron detectors is much higher. The traces we are looking for are traces of α -particles and Li-nuclei, which are very similar. The problem here is the natural α -radiation which the detectors cannot be shielded from completely during all stages of their processing. We tested detectors of different production batches, storage times and treatments as to their background level, see 3.6. Detectors 1 to 6 are all from a production from 2003 and have been stored in an aluminium bag for approximately one year before they were read out. All of them have been irradiated or left at the ILL at the same time. Detector 7 was produced in 2004 and only stored for about one month.

Detector	Irradiation status	Background traces per mm^2
1	Partially irradiated with UCN	3
2	Partially irradiated with UCN	4
3	Partially irradiated with UCN	11
4	Partially irradiated with UCN	5
5	Partially irradiated with UCN	4
6	24h above the reactor at ILL	1
7	Partially Irradiated with UCN	5

Table 3.6: Background measurements of various detectors

The aluminium shielding is quite effective and the natural α -radiation does not pose a difficulty. High background values seem to be developing during the irradiation process itself, probably caused by scattered neutrons. This background, under normal circumstances, is similar on all detectors and therefore easy to correct for. The extremely high background on detector 3, on the other hand, may have been caused by some kind of pollution with Actinium 228, a source of α -radiation, which was detected in a spectrometric analysis of the detectors at the ILL. Where this could have come from, we have no idea.

3.8 Reading out the detectors

Once the detectors have been etched the α -traces are visible under a microscope. The necessary magnification depends on the magnitude of the etching process. If a high resolution is considered imperative it is best to

etch away as little as possible. If the signal/background relation is more important it can be useful to etch away more of the bulk of the detector to make it easier to distinguish the real traces from defects in the material.

We used two standard optical microscopes each fitted with a CCD camera and an electronically steered stage to take photographs of the interesting areas of the detectors. One of the systems was developed within our group ([Luk042]) the other by MedXP, Gelsenkirchen. We then tried to develop computer programs to automatically identify and map the traces but this has not been successful yet. The problem is that under normal circumstances there are many small dust particles and water drops on the surface of the detectors. These irregularities are easy to distinguish from the traces by eye because of their shape and intensity but so far we were not able to teach a computer how to do this with sufficient accuracy.

Once the coordinates of the traces have been obtained there are corrections to make. Firstly, the detector could have been inclined with respect to the axis of motion of the microscope stage and secondly, during the etching process, the detector can become a little curved. These effects will worsen the resolution of the detector and have to be compensated for. A discussion of the correction methods is given in chapter 2.

Chapter 4

A quantum mechanical determination of the earths gravitational acceleration

The shape of the wave functions and the energy of the bound states in the gravitational potential are naturally influenced by the strength of the gravitational force. It is therefore possible to determine g from our experimental data.

4.1 Fitting g

The strength of the gravitational force is critical for the transmission of neutrons through our waveguide, because it defines the shape of the wave functions (for more detail see section 1.2):

$$\phi(z, n, g) = Ai(\zeta - \epsilon_n), \text{ where } \zeta = \frac{z}{R} \text{ with } R = \left(\frac{\hbar^2}{2m^2g} \right)^{\frac{1}{3}}, \quad (4.1)$$

This is straightforward to understand: A stronger force will "compress" the wave functions, i.e. the airy functions would become steeper and the neutrons would have a lower probability to be found at greater heights and inside the scatterer, see figure 4.1. This means that neutrons in each state could pass the waveguide earlier than they could have done with a comparatively weaker force. Classically this is no problem at all: the neutrons would just loose more energy travelling upward and because of energy conservation they could then only reach smaller heights. On the other hand, if the gravitational force was smaller less neutrons could pass

the waveguide because they would have a higher probability to be found at greater heights, in contact with the absorber. Then, for a bigger gravitational attraction the transmission through the waveguide would set in at a lower height, for lesser attraction at a greater height. For a stronger gravitational force this is illustrated in figure 4.2 where the theoretical curves are plotted together with data obtained from a transmission measurement in 2002.

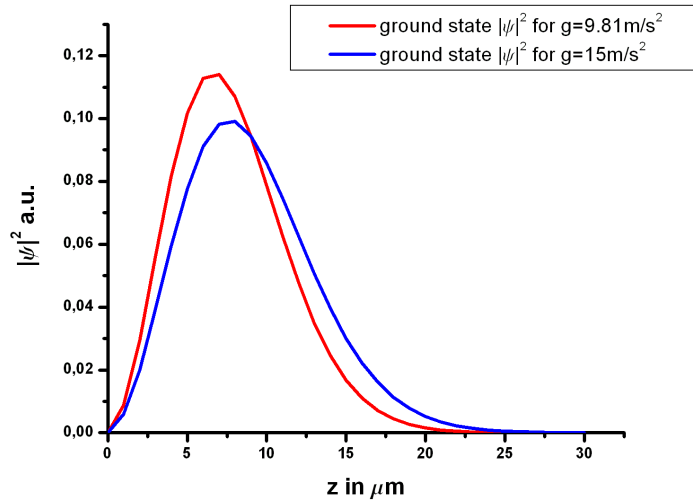


Figure 4.1: Normalized absolute square of ground state wave functions for different g

To determine g from our experimental data, we now varied its value in our quantum mechanical model for the transmission of neutrons through the waveguide, thereby changing the shape of the wave functions. We compared the predictions (with the gravitational constant g and the overall amplitude as free parameters) to the experimental data from 2002 and extrapolated the best fit g and its error to be $(g = 9.8 \pm 0.2) \frac{m}{s^2}$, see figure 4.3.

This result is very pleasing since it is one of the few quantum mechanical determinations of g and one of the very few that were performed by basically measuring the shape of the bound state wave functions. Other quantum mechanical measurements have achieved relative accuracies of $10^{-9}g$, [McGu02]!! These experiments employ interferometry of atoms or neutrons and are designed to have a high sensitivity. Our experiment, on the other hand, was not designed to determine the magnitude of the grav-

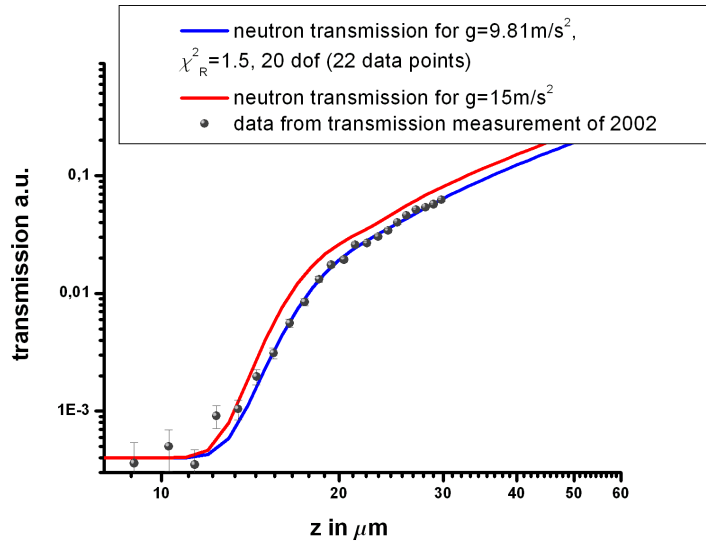


Figure 4.2: Predicted transmission through the waveguide for different g together with data from an experiment of 2002

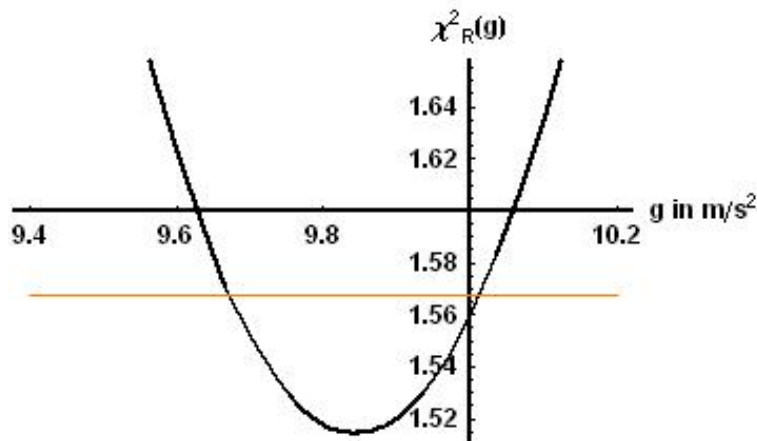


Figure 4.3: χ^2_R for the transmission prediction as a function of g , where the scattering parameter α_{loss} was fitted for $g = 9.81\text{m/s}^2$ and then kept constant

itational potential with a high accuracy since our priority has always been to prove the existence of bound quantum states in this potential no matter whether g is equal to 9 or 10 m/s^2 . Therefore, we would have been pleased with a relative accuracy of 10%, too and to achieve a relative accuracy of 2% is very encouraging, indeed!

The measurement can not be considered an absolute determination of g since it was not clear how the efficiency of the scatterer, α_{loss} , could be determined. From the first, approximate analytical calculation of this parameter we obtained a value that had to be multiplied by a factor of 1.6 to fit the data, [We04].

If the value of α_{loss} is treated as a free parameter we obtain $(g = 5.4 \pm 4.4) \text{ m/s}^2$, see figure 4.4. However, treating α_{loss} as a free parameter goes against the physical reality of the scattering process since its value is determined uniquely by the surface properties of the scatterer, independently of g . So the reason for this rather disappointing result is not a lack of experimental accuracy but the lack of a full theoretical description of the scatterer involved in the measurement, see chapter 1.

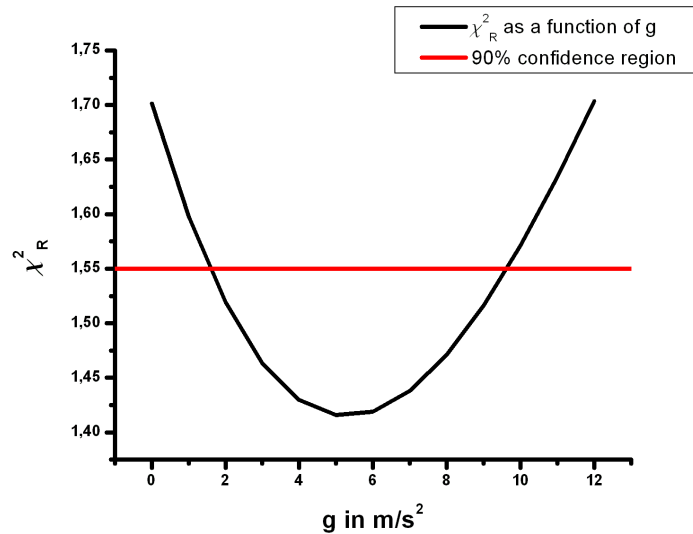


Figure 4.4: Fitting curve for g with 90% confidence interval

The value of α_{loss} has a great impact on the transmission curve and can partially compensate for the change in the overlap due to a compression of the wave function. Figure 4.5 shows the same data and transmission prediction for $g = 15 \text{ m/s}^2$ as figure 4.2 together with the theoretical transmission prediction for $g = 15 \text{ m/s}^2$ where α_{loss} has been fitted to the data.

This clearly shows the large effect that the scattering parameter has on the prediction: A sufficient adjustment of this parameter can alter the transmission function so that it correctly describes the data points for larger slit-widths. This is possible even though $g = 15m/s^2$ has been excluded by our result ($g = 5.3 \pm 3.7$) m/s^2 presented in figure 4.4.

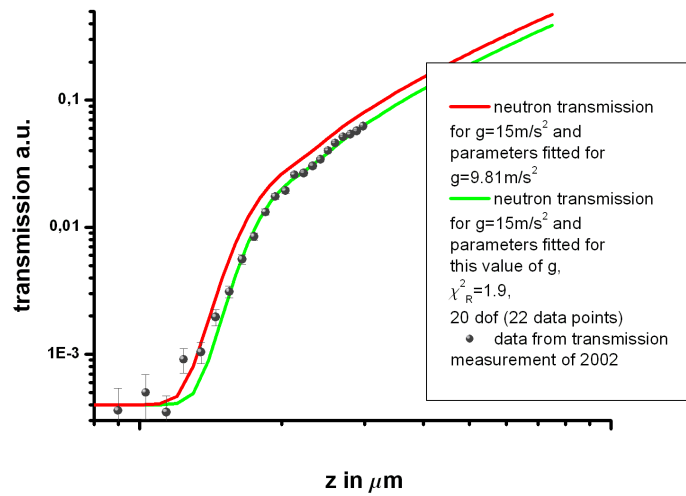


Figure 4.5: Predicted transmission for $g = 15m/s^2$ with and without the scattering parameter fitted to the data

Chapter 5

Testing for deviations from Newtonian gravity

With this experiment we are measuring gravity at very small distances. We could therefore, potentially, detect effects from gravity-like forces acting on very small length scales. Forces like this have been predicted by several theories that understand themselves as extensions of the standard model of particle physics, usually the with ultimate goal of finding a quantized theory of gravitation. Limits for the strength and range of these new forces have been predicted by our experiment and are published in [Abe03] and [Pro04]. Here we present further systematic checks of the different behaviour of attractive and repulsive forces. We also explore the effect of a systematic error in the calibration of the scatterer height by investigating the change in the derived limits for datasets that have been shifted by $1\mu\text{m}$ up or down in the vertical direction.

5.1 Introduction

Gravity is certainly a very well investigated physical concept and aspects like the equivalence principle and the inverse square law appear to be so close to solid facts as makes no difference. But actually, for distances smaller than 10^{-4}m not much is known. There has been a renewed interest in gravity because, in this range, extensions of the standard model predict new forces or deviations from the inverse square law due to extra dimensions, [Ark99].

There are many different models like this with different physical concepts behind them. Luckily, there are two main categories in which these models can be grouped according to their properties in the non-relativistic

limit. There is a large class that can be investigated starting from the addition of a Yukawa-potential to the Newtonian gravitational potential. These extra forces can be generated in theories with compactified extra-dimensions or by the exchange of light bosons such as for example scalar axions,[Fis99]. The gravitational potential then looks like

$$\phi(r) = -G_4 \int d^3r' \frac{\rho(\vec{r}')}{|\vec{r} - \vec{r}'|} \left(1 + \alpha e^{-\frac{|\vec{r} - \vec{r}'|}{\lambda}} \right) \quad (5.1)$$

In this formula α would be the strength of the so called "fifth force" compared to the strength of Newtonian gravity. λ is the range of the force.

Another class of theories predicts power-law corrections to the Newtonian potential. These can also be generated in extra-dimensional theories where the extra dimensions are not compactified but warped. Another possibility for power-law corrections to arise would be the simultaneous exchange of two massless scalars.

Personally, we are especially interested in forces with a range comparable to the dimensions of the bound states of our neutrons, i.e. in the μm range. This simplifies matters since the neutrons would only "feel" the extra force from the mirror and the scatterer but not from the rest of the setup and the planet. This situation is interesting because effects like this have been predicted recently by theories involving so-called large extra dimensions, [Ark99]. Additionally, there are comparatively few experiments like ours from which limits for additional forces with ranges between 1 and 3 μm can be deduced.

It has been known for a long time that using an additional, 5th dimension is one way to describe general relativity and electromagnetism by a single theory, [Kal21]. At roughly the same time it was also discovered that the same method can be used to unify electromagnetism and quantum theory, [Kle26]. Since then extra dimensions have been used extensively, either as a direct method to unify fundamental interactions or as the outcome of other theories with the same goal which can only be renormalized including higher dimensions.

Until quite recently it was believed that these extra dimensions would have to be compactified with radii corresponding roughly to the Planck lengths

$$L_P = \sqrt{\frac{G\hbar}{c^3}} = 1.6 \cdot 10^{-35} m, \quad (5.2)$$

and that only at this scale from the Inverse Square Law due to quantum effects would appear. It has then been realized that there is a theoretical

possibility to have extra dimensions with compactification radii even in the mm range. In these models gravity is the only fundamental force that has access to the large extra dimensions. All the other forces are localized on a four dimensional brane together with the particles of the Standard Model. This is done to explain why the Standard Model particles cannot feel these large extra dimensions.

In theories like this the strength of the additional Yukawa force is normally comparable to that of Newtonian gravity. There is the possibility, however, to have additional gauge fields which generate forces much stronger than gravity at distances the size of the large extra dimensions. This can work if the corresponding gauge bosons can penetrate all of the extra dimensions whereas the matter charged under this gauge group is stuck on the 4d brane together with the Standard Model. The ratio of the repulsive force mediated by the new gauge field to the gravitational attraction is, [Ark99],

$$\frac{F_{Gauge}}{F_N} \approx 10^6 \left(\frac{g_4}{10^{-16}} \right)^2, \quad (5.3)$$

where g_4 is the four dimensional coupling of the new interaction. The gauge boson must get a mass m_g which can be small enough to predict a Yukawa-addition to the gravitational force exactly in the interesting range of our experiment where $\alpha = g_4$ and $\lambda = m_g^{-1} \approx 1mm$.

To falsify this and other theories it is vital to investigate gravity across distances smaller than $10^{-3}m$ which is exactly what we have been doing.

The limits set by other groups measuring deviations in Casimir and Van-der-Waals forces, [Fis03], or changes in the frequencies of mechanical oscillators, [Hoy04], [Long03], can be seen from figure 5.1 which was taken out of [Hoy04]. For values of λ above $3\mu m$ these limits are orders of magnitudes below what we can observe with our experiment. However, below this value there is a gap which we might be able to fill. This is discussed in section 5.4.

5.2 The Yukawa potential for our setup

As indicated in the introduction to this chapter we are interested in short range forces that the neutrons will only "feel" to be coming from the mirror and the scatterer of the waveguide instead of the whole setup. The potential for our setup must therefore include the Newtonian gravitational potential and two Yukawa terms, one from the mirror and one from the scatterer at height h :

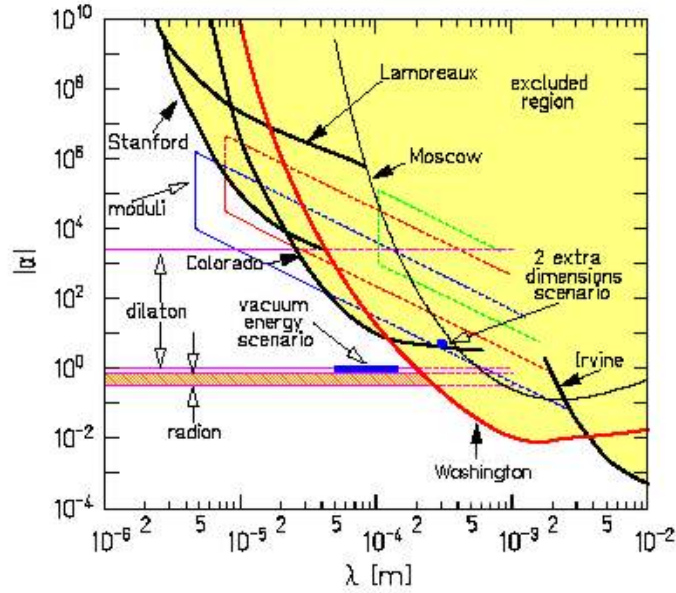


Figure 5.1: Current limits on the fifth force

$$\phi_{tot}(z) = g \cdot z - 2\pi \cdot \alpha \cdot \lambda^2 \cdot G_4 \cdot \rho_0 \cdot \left(e^{-\frac{z}{\lambda}} + e^{\frac{z-h}{\lambda}} \right). \quad (5.4)$$

For a detailed calculation see [We01].

If the Yukawa potential is attractive there would be small potential "pockets" directly at the mirror and the scatterer in which the neutrons could be "pulled in". For smallish pockets the wave functions will be stretched a little and the energies of the bound states will be shifted down. If the pockets got big enough they could change the entire behaviour of the system. The ground state would then have a much lower energy and would appear only inside the pocket. For a repulsive Yukawa potential the neutrons would be pushed into the center of the waveguide away from the mirror and the scatterer. The wave functions would be compressed and the eigenenergies shifted up. This is shown in 5.2. In this figure only the effect of the Yukawa potential of the mirror is visible.

These changes in the shape of the neutrons wave functions would, of course, also influence the transmission through the apparatus. The decisive factor here is the fifth force coming from the scatterer because it will significantly change the overlap of the neutrons wave functions with the scatterer. For an attractive force the transmission would then be lower

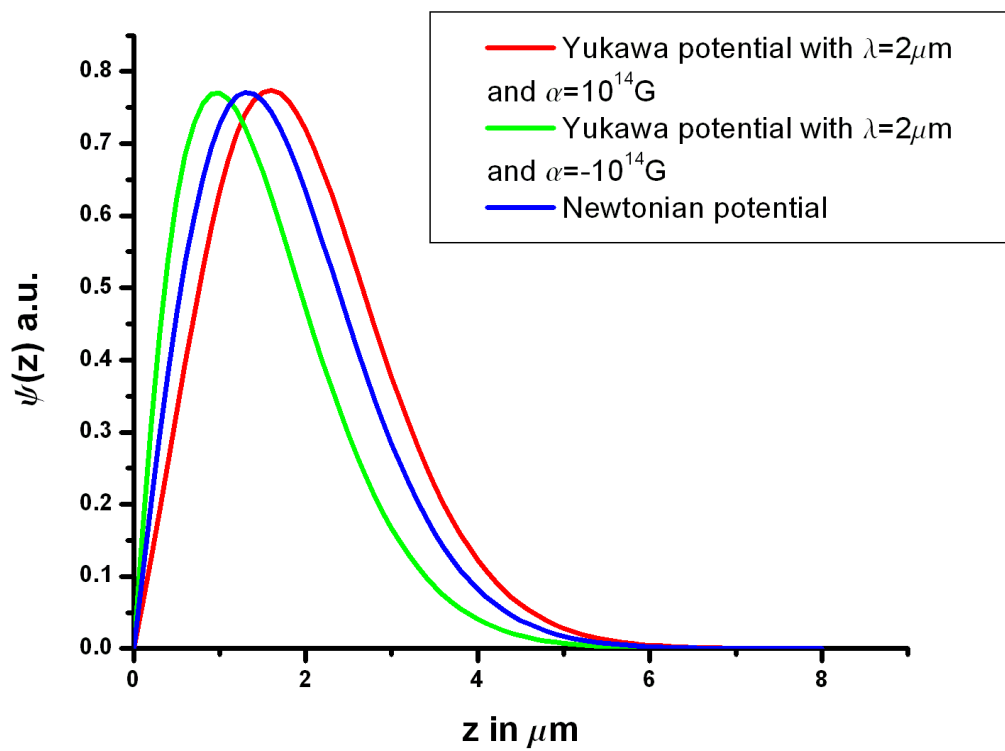


Figure 5.2: Comparison of the wave functions with and without an additional Yukawa potential

than the Newtonian expectation, for a repulsive force it would be higher, see 5.3

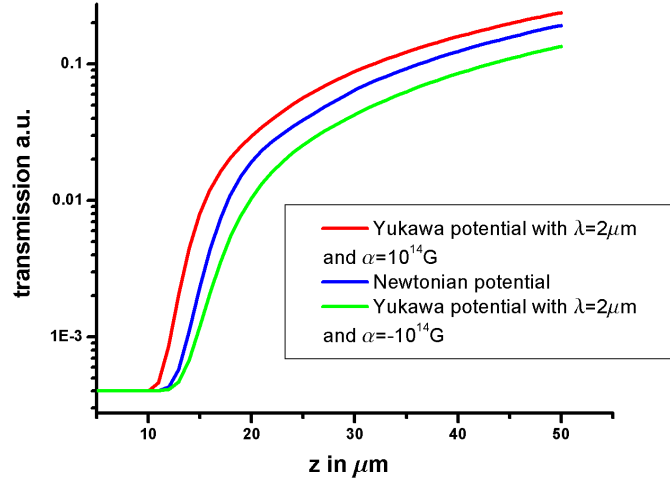


Figure 5.3: Comparison of the Transmission of neutrons through the waveguide with and without an additional Yukawa potential

5.3 An Estimation of possible limits for the parameters of the Yukawa potential

The first thing that was done within the frame of this thesis to actually establish whether or not it would make sense to try and set limits for potential extra forces was to look again at our determination of g , discussed in chapter 4. Presuming that there are extra, Yukawa-type forces around would be the same as to say that the effective g should differ from 9.81... This effective g should look like this:

$$g_{eff} = g_N + g_{Yuk}(z, \alpha, \lambda), \quad (5.5)$$

where

$$g_{Yuk}(z, \alpha, \lambda) = 2\pi \cdot \alpha \cdot \lambda^2 \cdot G_4 \cdot \rho_0 \cdot \frac{1}{z} \left(e^{-\frac{z}{\lambda}} + e^{\frac{z-h}{\lambda}} \right). \quad (5.6)$$

It is biggest at the mirror and at the scatterer where the fifth force is strongest. Since we are only interested in a crude estimation of the ef-

fects, at the moment, we can ignore the force coming from the mirror and concentrate on the potential of the scatterer, which has the dominant influence on the transmission. To make the estimate even cruder we will use the value of the potential at the scatterer as g_{Yuk} and assume that λ has the same order of magnitude as the width of the waveguide. This leaves us with:

$$g_{\tilde{Y}uk}(\alpha, \lambda) = 2\pi \cdot \alpha \cdot \lambda \cdot G_4 \cdot \rho_0. \quad (5.7)$$

Our measured g was: $g = 9.8 \pm 0.2$ (for constant fit parameters), i.e. we have achieved a relative accuracy of roughly 2%! If we now assume that we measured an effective g including a Yukawa force we can immediately deduce what kind of limits we might be able to set on the parameters of the Yukawa potential. It is clear that we could, at best, measure an extra acceleration with 2% the magnitude of g_N . The classical gravitational acceleration is given by

$$g_N = \frac{GM_E}{R_E^2} = \frac{4}{3}\pi G\rho R_E, \quad (5.8)$$

and we are interested in $g_{\tilde{Y}uk}$ divided by g_N :

$$\frac{g_{\tilde{Y}uk}}{g_N} = \frac{3}{2}\alpha \cdot \frac{\lambda}{R_E}. \quad (5.9)$$

We could theoretically detect a 2% effect which means that for the earths radius being approximately $10^7 m$ and a λ of $10^{-6} m$ we could exclude fifth forces with a strenght α of 10^{11} or more.

This method is nowhere near perfect, of course, and the actual effect of g_{Yuk} would be less than we estimated here. To really set limits for possible α and λ values it will be necessary to explicitly calculate the change of the wave functions and energy eigenvalues due to the additional force. This was done and will be presented in the next section.

5.4 An investigation of systematic effects on our limits for α and λ

The change in the wave functions and energy eigenvalues under the influence of various Yukawa potentials with different parameters was calculated numerically. Predictions for the transmission of neutrons through the waveguide were made for all pairs of "fifth force" parameters and fitted to the data from the 2002 experimental run. χ^2 values were calculated

for each fit. For each value of λ a function χ^2 of α was interpolated. Finally the 90% confidence interval of α for a certain value of λ was determined and the $\alpha(\lambda)$ curve for the boundary of possible values of α and λ was interpolated from these values.

In this chapter we will discuss the different effects of attractive and repulsive Yukawa potentials, the effect of a systematic error in the data as well as the impact of the parameter α_{loss} used to describe the quality of the scatterer used in the experiment. The scatterer can be modeled by a WKB calculation without a fit parameter starting from the Fermi potential of an absorbing layer on the surface of the scatterer, [We01]. When it was experimentally determined that the presence of an absorbent coating does not influence the efficiency of the scatterer the WKB model was not explored further. The model that was used for calculations within this thesis uses s-wave scattering at the rough scatterers surface as the dominant loss mechanism. This model requires a parameter, α_{loss} to account for the efficiency of the scatterer, [We01]. An attempt to calculate α_{loss} from first principles ([We04]) deviates from the fitted value by 60%.

Here, we investigate systematic effects of the hypothetical existence of so called "fifth forces" on the experiment and data. For the most part the fits presented were obtained with α_{loss} kept constant at the value obtained from a fit of the "Newtonian" prediction (without Yukawa forces) to the 2002 data. As we are investigating systematic effects and we know that the true value of α_{loss} is independent of Yukawa forces (it is defined by the geometry and material of the scatterer) this procedure is legitimate.

5.4.1 Observation of different effects for attractive and repulsive Yukawa potentials

In the process of this thesis we concentrated mostly on a repulsive Yukawa potential, i.e. positive α , since we assumed that the effects of an attractive and a repulsive potential of the same magnitude should be symmetrical in the range where no extra states can be formed inside the attractive Yukawa pocket. This is not quite the case as can be seen from figure 5.4

For a specified range of the potential the gradient of $\chi^2(\alpha)$ is greater for negative α than for positive α . This is an effect of the scatterer which we used in the experiment to filter out neutrons with high vertical velocities. The Airy functions of the bound states decrease exponentially with z . The attractive Yukawa potential at the scatterer will decrease the slope of the bound state wave functions and therefore increase the overlap of the absolute square of these wave functions with the scatterer. The repulsive

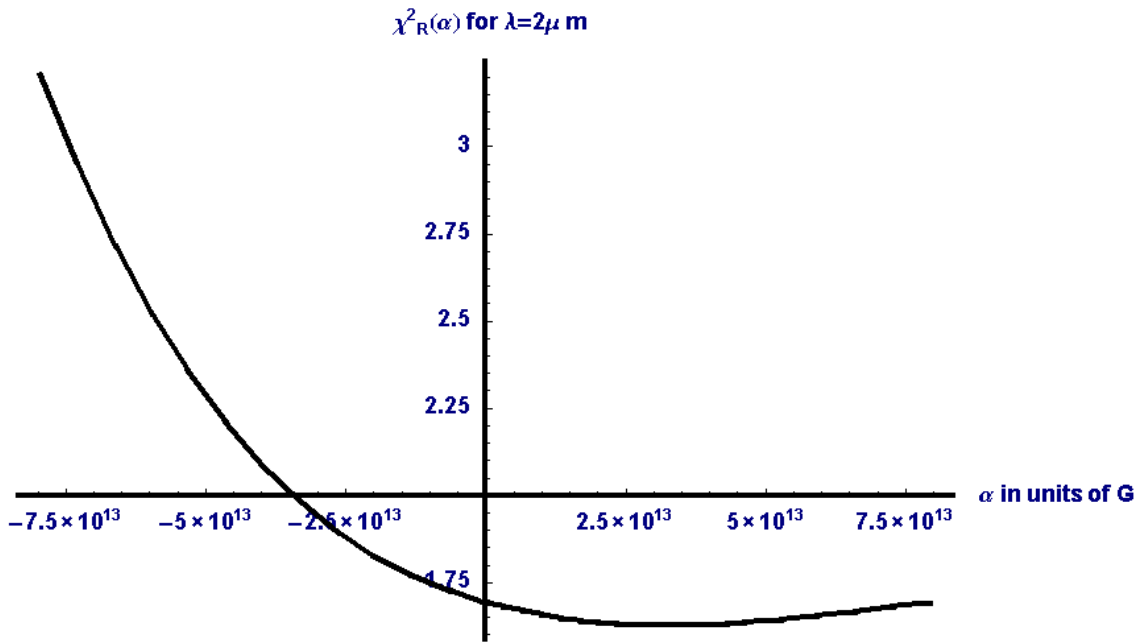


Figure 5.4: χ^2 for $\lambda = 2\mu\text{m}$ as a function of α

potential will increase the slope and decrease the overlap. Because of the exponential decrease of the wave functions the overall *change* in the overlap will be greater for an attractive potential. Thus, the limits on negative α for a certain value of λ are smaller than for positive α , see figure 5.5. The tooth in both curves at a λ value of roughly $3\mu\text{m}$ are due to interpolation instabilities.

5.4.2 Effects of a systematic error of the data

This position uncertainty leads to systematic effects which are demonstrated in figures 5.6, 5.8 and 5.7. In these figures the data has been systematically changed, once all data points have been moved up one micron and once down. The scattering parameter α_{loss} for each data set has been determined by fitting the Newtonian prediction with no Yukawa potentials present to each of the three data sets. When the data points are moved up this corresponds to the transmission setting in at greater heights which would also be the case if the wave functions were broader. This situation would favour an attractive Yukawa potential since this potential would lead to a "stretching" of the wave functions. When the data points are

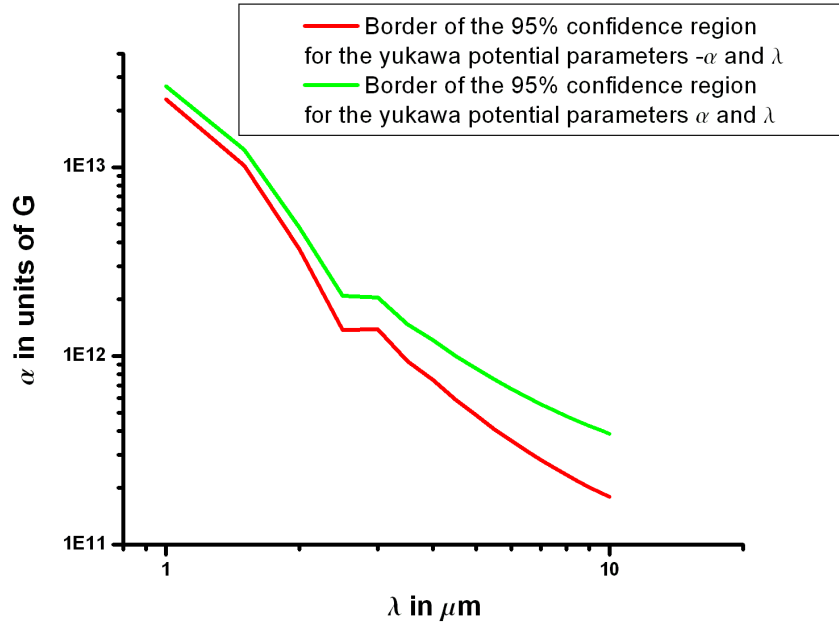


Figure 5.5: Comparison of the limits for positive and negative α

moved down this would accordingly favour a repulsive Yukawa force, because it would imply wave functions that are somewhat more narrow than those calculated from the Newtonian potential.

From figure 5.6 and the small section of figure 5.6 that is shown in figure 5.7 we can see that the limits set for the Yukawa parameters are tightest for the dataset where all data points have been moved up by one micron. This makes sense because we have calculated the curve for the parameters of a repulsive Yukawa potential which has an effect contrary to this particular displacement of the data.

From the qualitative argument given above for the correlation of the displacement of the data and the shape of the wave functions we would expect the limits for the dataset where all data points have been moved down by one micron to be higher than those derived from the original data, since the situation would favour an attractive Yukawa potential. This is not the case as we can see from figures 5.6 and 5.7 and we do not, yet, understand why not.

Figure 5.8 shows the same curves as figure 5.6 for $\lambda \approx 1 \mu m$. We can see that the curves for the different data sets are not parallel for $\lambda \leq 1.2 \mu m$. This effect can also not be understood from our hand-waving argument

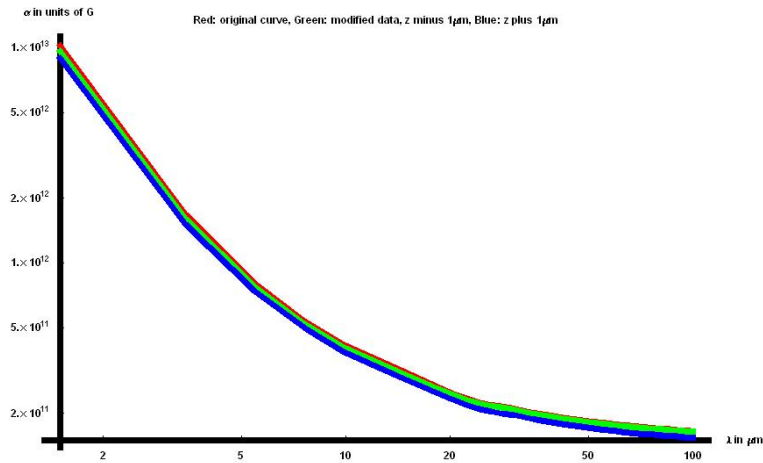


Figure 5.6: Change of the limits due to systematic errors in the measurement of the height of the absorber

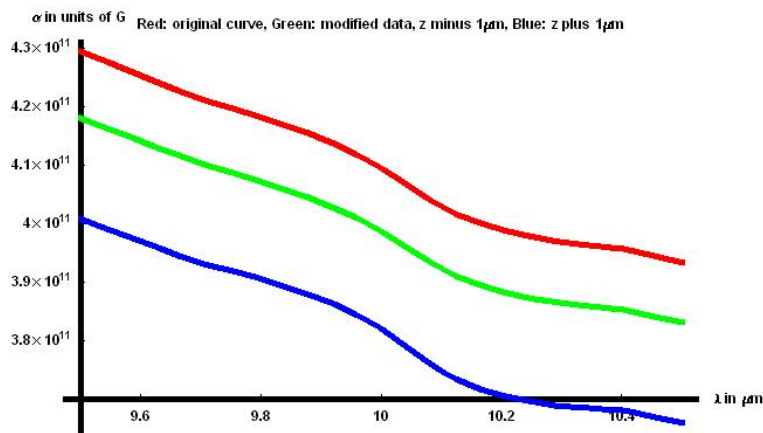


Figure 5.7: Change of the limits due to systematic errors in the measurement of the height of the absorber for λ around $10 \mu\text{m}$

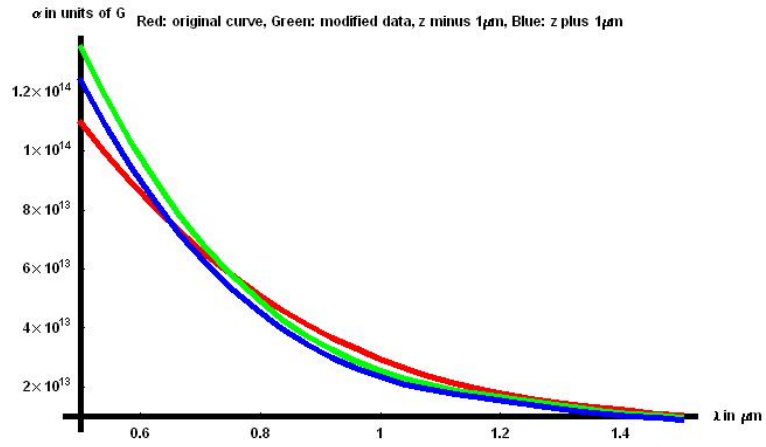


Figure 5.8: Change of the limits due to systematic errors in the measurement of the height of the absorber for λ around $1\mu\text{m}$

for the correlation of the Yukawa parameters and the displacements of the data. We assume that it is caused by instabilities of our model for the calculation of the eigenfunctions of the Schroedinger equation with an additional Yukawa potential, since for high values of α the numerical calculations converge very slowly.

Chapter 6

Summary

In the progress of this thesis a position sensitive neutron detector was developed. It has a very good spatial resolution of $1.4\mu m$ which is much higher than that of ordinary position sensitive neutron detectors, where the resolution usually lies between $100\mu m$ and $1mm$.

The new detector was tested this summer at the Institute Laue Langevin, Grenoble in an experiment to detect gravitationally bound quantum states of ultra-cold neutrons. It will be used regularly for this experiment from now on.

In this experiment ultra-cold neutrons with vertical energy components of the order of peV are stored above a horizontal mirror where they form bound quantum states in the gravitational field. A scatterer is placed some distance ($\approx 50\mu m$) above the mirror in order to remove neutrons with comparatively high energies. There are two methods of measuring the shape of the bound state wave functions: One is to move the scatterer upwards in small steps and to measure the transmission of neutrons through the slit between mirror and scatterer for each height of the scatterer. With this method it was possible to prove, for the first time, the existence of such states, [Ne02]. The other method is to leave the scatterer at a constant height and to directly measure the density distribution of the neutrons above the mirror. The position sensitive detector was used in such a measurement during the experimental cycle of this summer.

The quantum mechanical prediction for the outcome of the measurement describes the data very well and the measurement can be considered to be a significant indication for the quantum behaviour of neutrons in our installation. The statistics of the measurement, however, were not yet good enough to exclude the classical case with a high probability.

During the next experimental run in February 2005 the measurement of the density distribution will be repeated with better statistics. It could

then be possible to finally exclude the classical case for the motion of the neutrons.

Furthermore, within the framework of this thesis, the gravitational acceleration of the earth g was determined from data of the first kind of measurement (the transmission measurement) obtained in 2002. We have determined g with a relative error of 2% from a fit to the quantum states which is a highly satisfactory result.

Another aspect of this work was the investigation of possible extra forces and their effect on our measurement. The possibility of the existence of gravity-like forces acting on ranges below 1mm is the outcome of many string-inspired theories using so-called large extra dimensions. Some of these theories predict effects that could be detected with our experiment, and limits for the strength and range of these new forces have already been deduced from our data.

During the last year several systematic effects of these new, hypothetical forces in our experiment were studied using data from the 2002 transmission experiment. Attractive forces would be more easily detectable by our experiment than repulsive ones due to the geometry of the setup.

The calibration of the absorber height has been improved for the experiments performed this summer and there has been some progress in calculating the efficiency of the scatterer analytically. This makes us certain that we will be able to obtain much stronger limits for the range and strength of possible extra forces once the new data has been evaluated.

Appendix A

A recipe for handling the detectors

When dealing with the detectors it is important to always wear plastic gloves, clean clothing and a hair net!

A.1 Cleaning

Ultrasonic Baths	20 min Benzinum	20 min Isopropanol	20 min demineralized water
------------------	-----------------	--------------------	----------------------------

Greater stains can be removed using e.g. cotton wool dipped into Benzinum. It is best to let the detectors air-dry.

A.2 Coating

The pressure inside the evaporation device should be no more than 10^{-6} bar when the evaporation process is begun. Usually it will take about 14 hours until this pressure is reached.

The quality of the coatings is better if the evaporation rate is quite low. 1 – 2nm per minute are advisable.

After the application of the coating the detectors should be allowed to cool down slowly for about four hours.

A.3 Storage

Once they are taken out of the evaporation device the detectors should be stored in a dry place, possibly a box with silica gel or something similar in it.

They should be shielded against neutrons and α -particles as well as possible. This can be done by keeping the box with the detectors inside in an aluminium bag with BF_4 -mats around the inside.

A.4 Removing the coating

The coating normally peels off in a ultrasonic bath with water after a few minutes. Sometimes 20% HCl solution was used in addition. It is no problem if some Boron is left on the detector when it is immersed in the NaOH solution: Boron reacts very strongly with the Na ions to form Borax salt which will dissolve very quickly.

A.5 Etching

All detectors were etched in 20% NaOH solution. The bulk etch velocity depends on the temperature very strongly, see 3.3 and 3.4. For the best resolution as little as possible should be etched off the bulk - if the detectors are being read out under a microscope with a magnification factor of 20 this means about $0.2\mu m$.

The etching was done using a laboratory hotplate with a magnetic stirrer. However, a water bath with automatic temperature control and some kind of stirring mechanism would be preferable.

A.6 Readout

The traces can be read out with a standard optical microscope. Both systems we used had a movable stage under the lens and were fitted with a CCD camera. In this way photographs of the detector can be taken and mapped later on. It is important to have the microscope and the detector as clean as possible.

Appendix B

Ultra-Cold Neutrons

Here, we are following the argument of [Go91]. UCNs are defined as neutrons with a mean energy below 100neV. This is the energy where, for most materials, neutrons will undergo total reflection from a surface under all angles of incidence because their energy is lower than the effective potential of the surface. The actual interaction of the neutrons with the nuclei of the material can be approximated by the interaction with the so called Fermi potential. This approach relies on the assumption that, outside the range of the interaction between a neutron and a nucleus, the wave function of the neutron will not be changed dramatically. Therefore, a new potential can be introduced to calculate the long-range effects of the interaction within the boundaries of perturbation theory, despite the fact that the neutron-nucleus potential is very strong. For the calculation of long-range effects the Fermi potential is equivalent to the actual potential of the interaction.

As a first approximation a nucleus as seen by a neutron forms a spherical potential well with radius R , the range of the interaction. For slow neutrons with $\lambda \gg R$ the scattered wave function outside the potential has the form of a spherical wave. The total wave function outside the well can then be written as the sum of the incoming, plane wave and the scattered, spherical one:

$$\psi(\mathbf{r}) \propto e^{i\mathbf{k}\mathbf{r}} + f(\theta) \frac{e^{ikr}}{r}. \quad (\text{B.1})$$

Inside the well the neutron wave function is proportional to $\sin(KR)$ with $K = \sqrt{\frac{2m(E+V)}{\hbar^2}}$. Since the boundary of the well forms a θ -function singularity the transition at the boundary has to be continuous in the wave functions and their first derivatives. This condition can be used to de-

termine $f(\theta)$. Because of the small range of the strong interaction and the large wavelengths of the incoming neutrons, the scattering is mostly s wave and the angular dependence of $f(\theta)$ can be ignored. $f(\theta) = -\alpha$ is the usual convention for the sign of the scattering constant. In this case the wave function outside the potential will approximately have the form of a straight line for $r < \frac{1}{k}$:

$$\psi(r) \propto 1 - \frac{\alpha}{r}. \quad (\text{B.2})$$

Then, α can be interpreted as the radius of a hard sphere which would produce the same wave function as the scattering potential for $r \gg R$. With $f(\theta) = -\alpha$ positive values of α correspond to spheres with a repulsive potential. The boundary conditions for the wave functions now yields

$$\alpha = R\left(1 - \frac{\tan KR}{KR}\right), \quad (\text{B.3})$$

so that we can see that α will actually be positive for most values of KR , corresponding to an effectively repulsive potential although the actual interaction is attractive.

The differential cross section of the problem is

$$\frac{d\sigma}{d\Omega} = |f(\theta)|^2 = \alpha^2, \quad (\text{B.4})$$

which defines the physical meaning of $f(\theta)$ and α . $f(\theta)$ is called the scattering amplitude and α the scattering length.

It is still necessary to find an expression for the potential U so that a perturbative solution of the Schroedinger equation will yield B.1 far away from the region of the interaction. The Schroedinger equation for the relative motions of the neutron and the nucleus should look like

$$-\frac{\hbar^2}{2\mu}\Delta_\eta^2\psi(\eta) + (E - U(\eta))\psi(\eta) = 0, \quad (\text{B.5})$$

with the relative coordinate $\eta = r - r_n$ and the reduces mass μ , where

$$U(\eta) = \begin{cases} -U_0 & \eta < \rho \\ 0 & \eta > \rho \end{cases}, \quad (\text{B.6})$$

with some distance ρ chosen so that $\rho \ll \lambda_n, \rho \gg a$ and $\rho \gg R$.

The potential U can be calculated from $f(\theta)$ using the Born approximation for $f(\theta)$:

$$f(\theta) = -\frac{\mu}{2\pi\hbar^2} \langle k_f | U | k_i \rangle = -\frac{\mu}{2\pi\hbar^2} \int d^3\eta U(\eta) e^{i(\vec{k}_i - \vec{k}_f) \cdot \vec{\eta}}. \quad (\text{B.7})$$

Since the range of the potential U is supposed to be much smaller than the wavelength of the neutron (which coincides with the demand that $f(\theta) = -\alpha$, a constant) this equation is reduced to

$$\alpha = -\frac{2\mu}{3\hbar^2} U_0 \rho^3. \quad (\text{B.8})$$

For the validity of the Born approximation it is required that the magnitude of the potential U_0 is much smaller than the energy of the neutron. Together with the above expression for α this yields the critical condition that $-k\alpha \ll 1$ which is usually satisfied. Now we know that it must be possible to find such a potential U to give the correct scattering amplitude f .

If U_0 is now expressed in terms of α and the relation

$$\int U(\eta) d^3\eta = -U_0 \frac{4\pi}{3} \rho^3 \quad (\text{B.9})$$

is used the Fermi potential in first order Born approximation can finally be obtained:

$$U_F(\eta) = \frac{2\pi\hbar^2\alpha}{\mu} \delta^3(\eta). \quad (\text{B.10})$$

This is, of course, only the Fermi potential of a single nucleus. If we want to look at the interaction of UCN with a whole surface of a certain material, we have to consider the combined Fermi potential of all present nuclei. In this case it is no longer appropriate to consider the relative coordinate and the reduced mass since the interacting nuclei are bound in some kind of lattice structure. The scattering length of a single, free nucleus that we used so far also has to be replaced by the bound scattering length $\alpha_B = \frac{m}{\mu}\alpha$ which will be referred to as α from now on. The combined Fermi potential of the nuclei of the surface then looks like

$$U_F(\vec{r}) = \frac{2\pi\hbar^2}{\mu} \sum_i \alpha_i \delta^3(\vec{r} - \vec{r}_i). \quad (\text{B.11})$$

If the material is now considered to consist of identical isotopes which are homogeneously distributed with a sharp edge the surface can be considered to form a potential step of height

$$V = \frac{2\pi\hbar^2}{m}N\alpha, \quad (\text{B.12})$$

where N is the number density of the material. For typical materials this potential lies in the range of 100neV.

Finally, the problem has now been condensed down to the quantum mechanical potential step and it is straightforward to see that neutrons with total energies below the size of the potential step will be reflected for all angles of incidence. This is the reason why UCNs can be used in so many interesting experiments. Their storage time is almost only limited by the neutron β -decay lifetime which makes them ideally suited to measure exactly this value. UCNs are also used in the experimental search for the neutron electric dipole moment, the electric charge of the neutron and precision measurements of the neutron magnetic dipole moment, as well as many other experiments testing fundamental physical concepts. And, of course, they are also used in the search for gravitationally bound quantum states.

Bibliography

- [Abe03] H. Abele, S. Baessler and A. Westphal, Lect.Notes Phys. **631** 355-366 (2003)
- [Ant98] I. Antoniadis et al., Phys. Lett. B **88**, 257 (1998)
- [Ark98] N. Arkani-Hamed et al., Phys. Lett. B **429**, 263-272 (1998)
- [Ark99] N. Arkani-Hamed et al., Phys. Rev. D **59**, (1999)
- [Cec01] S. Cecchini et al., Radiat. Meas. **34**, 55, (2001)
- [COW75] R.Colella,A.W. Overhauser and S.A. Werner, Phys. Re. Let. **34**, Number 23, 1472 (1975)
- [Fis99] E. Fischbach and C. Talmadge, The search for non-Newtonian gravity (Springer-Verlag, Berlin, 99)
- [Fis01] E. Fischbach et al., Phys. Rev. D **64**, (2001)
- [Fis03] E. Fischbach et al., hep-ph/0310157
- [Flei75] R.Fleischer et al., Nuclear Tracks in Solids,(Univ. California Press, 1975)
- [Flor99] E. Floratos and G.K. Leontaris, hep-ph/9906238
- [Flü99] S. Flügge, Rechenmethoden der Quantentheorie (Springer-Verlag, Berlin, 1999)
- [Go91] R. Golub et al. Ultra-Cold Neutrons, (Adam-Hilger, Bristol, 1991)
- [Hoy04] C. D. Hoyle et al., hep-ph/0405262
- [IC00] Intercast Europe S.p.A., <http://www.df.unibo.it/macro/intercast/charact.htm>
- [IC01] Intercast Europe S.p.A., Product Information Sheet

- [Kal21] T. Kaluza, Sitz. Preuss. Akad. Wiss., p. 966 (1921)
- [Kle26] O. Klein. Quantentheorie und fünfdimensionale Relativitätstheorie. Z. Phys., 37:895, 1926.
- [Klei01] M. Klein et al., PSND 2001
- [Krau01] D. Krause and E. Fischbach in Gyros, Clocks and Interferometers...: Testing Relativistic Gravity in Space, edited by C. Lammerzahl, C. W. F. Everitt, and F. W. Hehl (Springer-Verlag, Berlin, 2001), pp. 292-309. hep-ph/9912276.
- [Leo94] W. Leo, Techniques for Nuclear and Particle physics, (Springer-Verlag, Berlin, 1994)
- [Long03] J. C.Long et al., Nature **421**, 922 (2003) and J.C.Long et al. hep-ph/0210004
- [Luk041] L. Lukovac, private communication
- [Luk042] L. Lukovac, master thesis, University Joseph-Furrier, Grenoble 2004
- [McGu02] J. M. McGuirk et al., Phys. Rev. A **65**, (2002)
- [Me76] A. Messiah, Quantenmechanik Band 1, (de Gruyter, 1976)
- [Ne02] V. Nesvizhevsky, H. Abele et al., Nature **415**, 297, (2002)
- [Ne03] V. Nesvizhevsky, H. Abele et al., Phys. Rev. D **67**, (2003)
- [Ne04] V. Nesvizhevsky, private communication
- [Pro04] V. Nesvizhevsky and K. Protasov, hep-ph/0401179
- [Rue00] F. Rueß, diploma thesis, University of Heidelberg 2000
- [Schmi04] U. Schmidt, private communication
- [Schrau04] J. Schrauwen, master thesis, FUNDP LISE, NAMUR Belgium (2004)
- [Schw98] F. Schwabl, Quantenmechanik (Springer-Verlag, , Berlin, 1998)
- [SRIM] J. Ziegler, SRIM 2003 (IBM-Research)
- [We01] A. Westphal, diploma thesis, University of Heidelberg (2001)
- [We04] A. Westphal, private communication